RMetS
Royal Meteorological Society

Internal processes within the African Easterly Wave system

D. Emmanuel Poan,* Jean-Philippe Lafore, Romain Roehrig and Fleur Couvreux
CNRM-GAME, Météo France and CNRS, Toulouse, France

*Correspondence to: D. Emmanuel Poan, CNRM-GAME, Météo France and CNRS, 42 Avenue Gaspard Coriolis, 31057 Toulouse, France. E-mail: emmanuel.poan@meteo.fr

The internal processes within an African Easterly Wave (AEW) system, involving mass, dynamic and water vapour fields are investigated using ERA-I reanalysis, in order to highlight the interactions between convection and AEWs. The budgets of heat, moisture and momentum are analysed during the different phases of AEWs detected using synoptic-scale precipitable water anomalies as proposed by Poan *et al.* (2013). The strong climatological meridional gradient of moisture present in the Sahel impacts the shape of the apparent heat source and humidity sink. AEW events over the Sahel are associated with a meridional shift of the intertropical convergence zone (ITCZ). Large exchanges of momentum by small-scale convective transport are also highlighted between the low- and mid-levels, contributing to the reinforcement of the AEW circulation at 600 hPa and the damping of the monsoon flow. This also appears as a possible mechanism for the vertical tilt of the meridional wind associated with AEWs. Heat budget computation, in the southern flank of the West African Heat-Low (HL) region where such AEWs occur, reveals that the heating anomalies are mainly driven by the horizontal advections. The vertical circulation acts as a precursor, which initiates the heat transport in the lower troposphere. However, weaker, turbulent mixing also participates in the development of these anomalies, especially in the boundary layer. These budgets ultimately allow the distinct contributions of diabatic and adiabatic processes to be determined.

Key Words: African Easterly Waves; dynamics; diabatic processes; convection

Received 28 November 2013; Revised 30 June 2014; Accepted 2 July 2014; Published online in Wiley Online Library

1. Introduction

From the pioneering studies to our current knowledge of African Easterly Waves (AEWs), more than 75 years have passed. However, their detection, comprehension and, most of all, their forecasting still challenge the scientific community. According to Fink's (2012) historical review, AEWs were first described by Piersig (1936) and Regula (1936) as 4–5-day-period disturbances of surface pressure on the Atlantic coast of West Africa. Regula (1936) noted strong oscillations of surface pressure, which were associated with squall lines, preferably occurring during the pressure rise phase. Piersig (1936) showed that these pressure disturbances were associated with the passage of a surface cyclonic transient circulation. Then, Hubert (1939) documented the zonal propagation of the waves, west-south-westward propagation at a speed of 6–14 m s^{-1}, using daily pressure maps within the 15–20°N band. He was the first one to establish a link between AEWs and tropical cyclones over the Atlantic. The first dynamical theory of AEWs came later with the pioneering work of Riehl (1954), who explained their dynamics in the Caribbean by using the conservation of potential vorticity. The following studies considered AEWs mostly from a dynamical perspective using the mid-level vortex or associated meridional wind for their detection. The Global Atmospheric Research Program (GARP) Atlantic Tropical Experiment (GATE) measurements in 1974 provided a unique observational dataset documenting AEWs. Among others, Burpee (1974) and Reed *et al.* (1977) described their dynamical characteristics (period, speed and wavelength) from ground-based observations and suggested that baroclinic and barotropic instabilities could explain the structure, growth and life cycle of AEWs. This was later confirmed by numerical studies (Thorncroft and Hoskins, 1994a, 1994b; Paradis *et al.*, 1995, among others). More recently, a few observational and numerical studies have discussed these theories, arguing for a more complex system (e.g. Hall *et al.*, 2006; Kiladis *et al.*, 2006). Barotropic–baroclinic instability alone is not able to explain the initiation and intermittency of AEWs, and a finite-amplitude initial perturbation is required at the entrance of the African Easterly Jet (AEJ) to trigger the waves (e.g. Berry and Thorncroft, 2005; Mekonnen *et al.*, 2006; Leroux and Hall, 2009). Diaz and Aiyyer (2013a, 2013b) also recently suggested an upstream development mechanism for AEW genesis, in which kinetic energy divergence from a pre-existing AEW can trigger a new wave while inducing the decay of the former one.

AEWs and convection are intimately linked over West Africa (e.g. Kiladis *et al.*, 2006). Investigating the geographical position of squall lines relative to the AEW phases, Fink and Reiner (2003) have found that, in the Sahel area (north of 12.5°N), convection is forced west of the ridge while it occurs more

frequently in the vicinity of the trough in southern West Africa (south of 12.5°N). This study corroborates previous findings of Burpee (1974), Duvel (1990) and Mathon *et al.* (2002a), who noted that convection was suppressed west of the trough in the dry region of the Sahel between 15 and 20°N. A few modelling studies have highlighted the importance of moist processes in AEWs. Cornforth *et al.* (2009), following Thorncroft and Hoskins (1994a, 1994b), found that convection significantly contributed to the growth of AEWs while slowing them down and reducing their meridional extent. Parker (2008) developed a linear dynamical model to describe the interactions between the AEWs and the soil moisture patterns in the northern Sahel as observed by the composite study of Taylor *et al.* (2005). However, the interactions over the Sahel of moist convection, boundary layer and surface processes with synoptic waves are still not well understood.

Over the Sahel, the amount of moisture is one of the most important limiting factors of convection. Therefore, our seminal idea, developed in Poan *et al.* (2013) (hereafter PRCL13) is to place humidity at the centre of the analysis of West African synoptic variability. During the pre-onset stage of the West African monsoon, Couvreux *et al.* (2010) found AEW-like structures associated with monsoon bursts using the atmospheric total column water vapour, also called precipitable water (hereafter PW). A detailed analysis of a case-study of an intense monsoon burst observed during the African Monsoon Multidisciplinary Analysis (AMMA) field campaign by Cuesta *et al.* (2010) and its simulation at high resolution (Barthe *et al.*, 2010) suggest favourable interactions with the passage of an intense AEW, the reinforcement of the cyclonic circulation in the Saharan Heat-Low (HL) ahead of the trough of the AEW, and cold pools generated by rain evaporation in mesoscale convective systems (MCS). More recently, PRCL13 documented the moisture footprint of AEWs propagating along the northern flank of the AEJ, using a composite analysis of synoptic 'wet' and 'dry' events detected according to PW anomalies. These events are remarkably frequent and their composite structure is very much like that of AEWs: westward propagation at a speed of 9 m s^{-1}, 5–6-day period, wavelength of 3800 km. Rainfall is strongly modulated during these events, highlighting a robust relationship between precipitation and PW at the synoptic time-scale. The analysis of the moisture budget during the wave life cycle also points out a balance between diabatic and adiabatic (linear and nonlinear) processes, which needs to be better documented and understood.

The aim of the present article is to document the interaction between convection and dynamics in AEWs. Previous studies focused mainly on the adiabatic loop between dynamics and the mass field but the understanding of the impact of diabatic processes is still lacking. In particular, the modulations of the apparent heat source (Q_1), the moisture sink (Q_2) and the apparent momentum source (Q_3) during AEWs deserve further documentation and investigation. Starting from the work presented in PRCL13 and its robust moisture-oriented detection and analysis of AEWs, the present article focuses on a detailed investigation of heat and momentum budgets. Data and methods are briefly described in section 2. Section 3 starts with an assessment of the mean meridional structures of the monsoon circulation and the associated convective activity. Then, a diagnosis of how diabatic contributions are modulated during the passage of the composite AEW is given. We also briefly investigate the relative contribution of the diabatic heating and large-scale dynamical forcing to the vertical circulation, using the Q-vector approach. Sections 4 and 5 present temperature and meridional momentum budgets over the Sahel area at the northern flank of the AEJ focusing on an analysis of the respective contribution of diabatic and dynamical processes. The main results of this article and suggestions for future investigations are summarized in section 6.

2. Data and methodology

2.1. Data

Most of the present study is based on the last ('Interim') European Centre for Medium-range Weather Forecasts (ECMWF) ReAnalysis (Dee *et al.*, 2011, ERA-I hereafter). Dee *et al.* (2011) showed that this reanalysis is a remarkable improvement over the former ECMWF ERA40, thanks to a better assimilation scheme. More specifically, the increase of satellite data assimilated (clear-sky radiance from geostationary satellites, passive microwave imagers over oceans) leads to a better representation of the hydrological cycle. Six-hourly outputs (0000, 0600, 1200, 1800 UTC) covering the 1989–2007 period at 0.75° × 0.75° horizontal resolution over 31 pressure levels are used hereafter. The ERA-I data provide wind, temperature, humidity, precipitable water and rainfall to describe AEWs and the related processes. The rainfall forecast of the reanalysis is, however, compared to Tropical Rainfall Measuring Mission (TRMM) data (see below) to assess the ability of the reanalysis to capture reasonable interactions between AEWs and convection. Note that, using independent ground-based Global Positioning System (GPS) retrievals of PW, PRCL13 demonstrated the good skill of ERA-I PW in detecting AEW events.

Observational rainfall estimates are provided by the TRMM multiplatform algorithm (TMPA). Version 3B42 of TRMM rainfall estimates is used here. It is available on a 0.25° × 0.25° spatial grid at 3-hourly intervals, and covers the period 1998–2007. The TRMM-3B42 (Huffman *et al.*, 2007) algorithm combines the native TRMM Precipitation Radar (an electronically scanning radar at 13.8 GHz) rainfall measurements with both passive microwave imager measurements (Special Sensor Microwave Imager (SSM/I), TRMM Microwave Imager (TMI), Advanced Microwave Scanning Radiometer for Earth Observing System (AMSR-E), and Advanced Microwave Sounding Unit-B (AMSU-B)) and geostationary satellite brightness temperature. For easier comparison with ERA-I outputs, TRMM rainfall estimates are cumulated to obtain 6-hourly precipitation time series (0–6, 6–12, 12–18 and 18–24 h). Roca *et al.* (2010) assessed the quality of TRMM rainfall over West Africa and concluded that TRMM-3B42 showed high skill in reproducing the ground network synoptic variability.

The composite analysis (see the next subsection) makes use of intraseasonal anomalies to remove the influence of the annual cycle. These are obtained as the difference between the observed raw value and that of the mean 6-hourly annual cycle. The diurnal cycle is further removed using a 24 h running average (four points). Further details are given in PRCL13.

2.2. Composite analysis of AEW

The composite analysis follows PRCL13. Dry and wet events associated with AEWs are detected using precipitable water averaged over the central Sahel domain (12–20°N, 5°W–5°E). This regional index is first 10-day high-pass filtered to focus only on synoptic events. PRCL13 showed that the average 5–6-day scenario comprised a dry phase, followed by the passage of the AEW mid-level trough leading to the wet phase, before the passage of the AEW mid-level ridge and a return to the dry phase.

While PRCL13 analysed wet and dry phases of AEWs separately (they were found to be mainly symmetrical), here we propose to focus on transition events, which have the advantage of increasing the signal-to-noise ratio in the composites and of placing AEW mid-level troughs and ridges (and thus the AEW itself) at the heart of the analysis. Isolated dry or wet events, which are rather infrequent (see appendix A), are thus removed from the present study. This small number of isolated events is consistent with previous studies (Carlson, 1969; Pytharoulis and Thorncroft, 1999; Diaz and Aiyyer, 2013a, 2013b), which suggest that AEWs tend to travel in groups or 'wave trains' of about three waves. In

consequence, only a subset of the dry and wet events of PRCL13 is considered to detect these dry-to-wet and wet-to-dry transition events. The only condition is that the transition should occur within a time window of 1.5–3 days. This provides a compromise between a sufficiently large sample for statistical significance and a focus on the most frequent transitions, which correspond to strong AEWs regarding their moisture footprint (see also appendix A). The reference time of the composite (called t_0) now represents the middle of these transitions and corresponds to the AEW mid-level trough in the case of a dry-to-wet transition event. The reference time for the composite 'wet' event (noted 'W' in the figures) will be t_0+ 1.25 and that for the 'dry' ('D') event t_0 - 1.25 days. Based on these transition events, any composite of a variable α will be noted α^*.

2.3. Heat, moisture and momentum budget analyses

In the present study, budgets of potential temperature, specific humidity and horizontal momentum within the AEW life cycle are computed and analysed with a focus on apparent sources due to diabatic processes as described below. They provide more precise representations of sources of heat, moisture and momentum due to processes occurring at time and space scales smaller than the time and space resolution of the ERA-I outputs (i.e. 6 h and 0.75°).

The concept of apparent heating source Q_1 and moisture sink Q_2 proposed by Yanai *et al.* (1973) allows these sources to be computed as residuals:

$$Q_1 = \overline{\pi}\left(\frac{\partial\overline{\theta}}{\partial t} + \overline{u}\frac{\partial\overline{\theta}}{\partial x} + \overline{v}\frac{\partial\overline{\theta}}{\partial y} + \overline{\omega}\frac{\partial\overline{\theta}}{\partial p}\right) \equiv Q_r + Q - \overline{\pi}\frac{\partial\overline{\theta'\omega'}}{\partial p}, \quad (1)$$

$$Q_2 = -\frac{L}{C_p}\left(\frac{\partial\overline{q}}{\partial t} + \overline{u}\frac{\partial\overline{q}}{\partial x} + \overline{v}\frac{\partial\overline{q}}{\partial y} + \overline{\omega}\frac{\partial\overline{q}}{\partial p}\right) \equiv Q - Q^{l-s} + \frac{L}{C_p}\frac{\partial\overline{q'\omega'}}{\partial p}, \quad (2)$$

where θ is the potential temperature, q is the specific humidity and u, v and ω are the zonal, meridian and vertical wind components respectively. $\pi = T/\theta$ is the reduced Exner pressure and L the specific latent heat of condensation. Q is the total latent heating due to phase changes between liquid/solid water and water vapour, while Q^{l-s} refers to the heating due to melting–freezing processes (Caniaux *et al.*, 1994a). Q_r is the radiative heating. For a domain of a given scale, primes denote subdomain fluctuations from the domain-mean state (overbars). The derived term $Q_1 - Q_2 - Q_r$ gives the vertical transport of moist static energy by small-scale eddies associated with both dry and moist convection and the heating due to melting–freezing processes (Q^{l-s}).

Similarly, the transport of momentum by small-scale processes is assessed with the apparent momentum source $\mathbf{Q}_3$ defined in Redelsperger and Lafore (1994). Its meridional component reads:

$$Q_{3,y} = \left(\frac{\partial\overline{v}}{\partial t} + \overline{u}\frac{\partial\overline{v}}{\partial x} + \overline{v}\frac{\partial\overline{v}}{\partial y} + \overline{\omega}\frac{\partial\overline{v}}{\partial p} - f\overline{u} - \frac{\partial\overline{\varphi}}{\partial y}\right) \equiv -\frac{\partial\overline{\omega' v'}}{\partial p}, \quad (3)$$

where f is the Coriolis parameter and φ is the geopotential. A similar equation is used for the zonal component $Q_{3,x}$. Note that Eqs (1)– (3) assume negligible horizontal fluxes.

As mentioned earlier, diabatic sources are representative of scales smaller than that of ERA-I outputs. In the following, these sources can be averaged over larger domains. They remain representative of the scale at which they were first computed, however. Two approaches can be used to derive apparent sources. The first one simply uses outputs from ERA-I forecasts, which provide 6-hourly Q_1, Q_r and Q_2 as a result of the model physical parametrizations. The second method is based on the computation of residuals using Eqs (1)–(3), where tendency, advection, Coriolis and pressure terms are computed at each grid point using the 6-hourly ERA-I outputs. In that case, the superscript 'res' will be used. In the latter case, the apparent sources Q_1^{res}, Q_2^{res} and $\mathbf{Q}_3^{res}$ contain contributions from (i) model physics, (ii) the assimilation increment, and (iii) spatial regridding. Whatever the method used, apparent sources depend on the model physics. The inclusion of assimilation increments should improve the quality of their estimates, as they mostly tend to correct physics deficiencies in the model. In the following, the ability of ERA-I to capture specific features of synoptic variability, in particular regarding relationships between dynamics and precipitation, provides confidence in the computed terms. In addition, although the two approaches yield slightly different estimates (e.g. Figure 8), the main conclusions remain robust. For the sake of brevity, most of the results presented hereafter use the residual approach. Finally, it should be noted that all these terms will be analysed in terms of their intraseasonal anomalies and composites, following the steps described in section 2.1 most of the time. The use of anomalies is intended to help remove the relatively large slower-scale errors, for instance the monthly ERA-I rainfall errors shown by Di Giuseppe *et al.* (2013), and provide insight into robust physical mechanisms.

3. Latitudinal modulations associated with AEWs

3.1. Climatological background

The West African Monsoon (WAM) is characterized by opposite meridional gradients of humidity and temperature (thick grey lines in Figure 1(b,c)). Moist, relatively cold air prevails over the Sudanese region, south of 12°N, inducing a low cloud base (∼900 hPa, thick line in Figure 2). Over the Sahara, north of 22°N, dry, warm air dominates, with an elevated cloud base (∼600 hPa). In between, the Sahel transition zone corresponds to maximum meridional gradients. South of 22°N, horizontal winds are characterized by a south-westerly monsoon flow between the surface and 800 hPa and a relatively weak reverse flow above (contours in Figure 2(b,d)). Above, the strong low-level baroclinicity yields the mid-level AEJ near 15°N ($-12\,m\,s^{-1}$ at 600 hPa, Figure 2(d): Thorncroft and Blackburn, 1999; Thorncroft *et al.*, 2003). Although the mean WAM meridional structure has been widely documented (e.g. Reed *et al.*, 1977; Lafore *et al.*, 2010), its counterpart in terms of diabatic heating and moistening has received less attention.

During the boreal summer, the southern subsiding branch of the regional Hadley-like circulation is located over the Gulf of Guinea, south of 5°N, (contours in Figure 2(a)), and leads to a dry mid- and upper troposphere (relative humidity contours in Figure 2(c)). Convective heating and drying are weak (shading in Figure 2(a,b)), while the large radiative cooling (~ -2 K day^{-1}, Figure 2(c)) balances the subsidence heating.

Over the Sudanese continental band (5–12°N), the ITCZ region corresponds to a deep convection area with strong large-scale vertical ascent, strong diabatic heating near 500 hPa (∼3 K day^{-1}) and strong diabatic drying near 650 hPa (∼2 K day^{-1}). Consistently, ERA-I precipitation (Figure 1(e)) is maximum at ∼ 8°N, slightly southward of the TRMM maximum precipitation (Figure 1(f)). North of 10°N, the $Q_1^{res} - Q_r$ vertical profile progressively becomes a stratiform structure characterized by heating above 650 hPa and cooling below. The maximum moistening follows the mean cloud base and the northward deepening of the boundary layer. This cooling and moistening region is probably driven by both boundary-layer dynamics and evaporation of precipitation.

North of 17°N, the Saharan heat-low region is driven by a deep, dry convective boundary layer, which extends up to ∼550 hPa

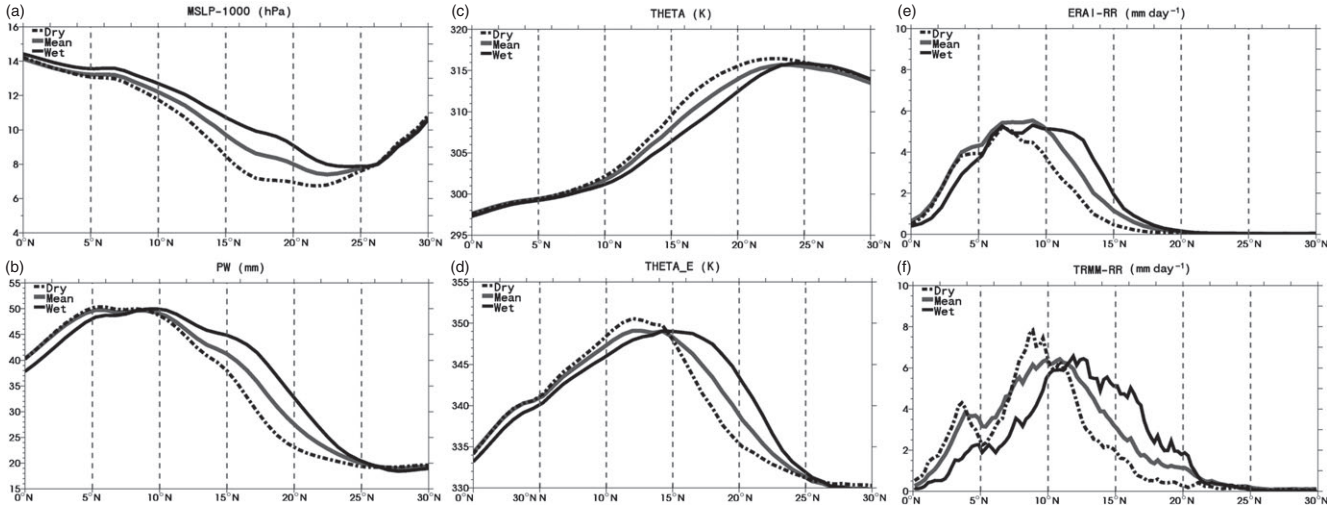

Figure 1. (2°W–2°E) Average meridional profiles of (a) mean-sea-level pressure (*MSLP*) (minus 1000 hPa), (b) *PW* (mm), (c) θ (K), (d) θ_e (K), (e) ERA-I rainfall (mm day^{-1}) and (f) TRMM rainfall (mm day^{-1}), for the JJAS (June–September) climatological mean state (thick grey lines), the composite *wet* phase (t_0+ 1.25 days, black solid lines) and the composite *dry* phase (t_0- 1.25 days, dashed-dotted lines).

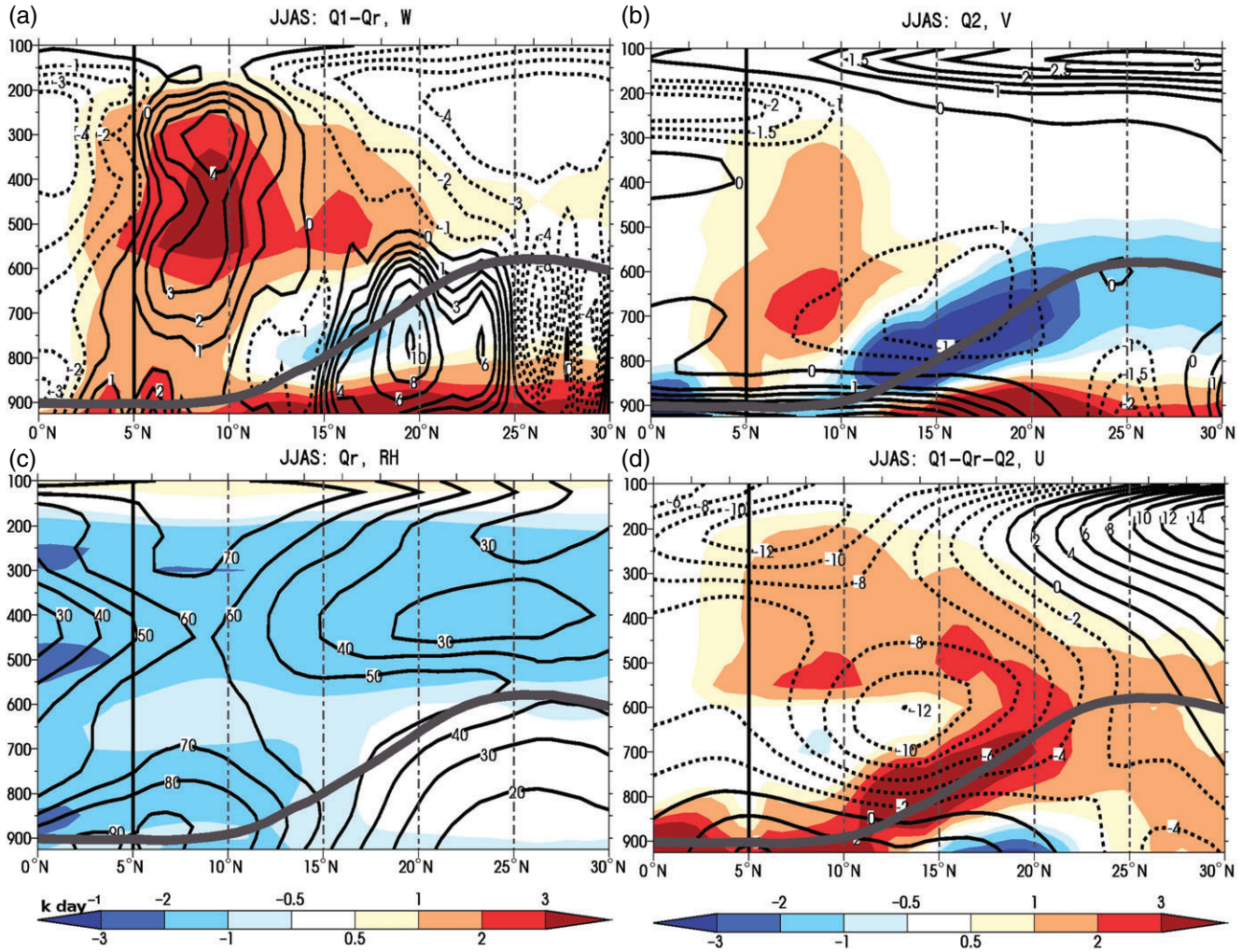

Figure 2. (2°W–2°E) Average meridional vertical cross-section in JJAS of (a) $Q_1^{res} - Q_r$ and W(mm s^{-1}), (b) Q_2^{res} and V(m s^{-1}), (c) Q_r and *RH* (%), (d) $Q_1^{res} - Q_2^{res} - Q_r$ and U (m s^{-1}). Q_i are in K day^{-1} (colours). The bold grey lines indicate the mean cloud base altitude diagnosed according to 2 m temperature and relative humidity.

with a strong large-scale low-level ascent capped by the subsiding branch of the regional northern overturning cell. As a result, surface pressure is minimum around 22°N (1007 hPa at mean sea level, Figure 1(a)) at the location of the intertropical discontinuity (ITD), defined as the surface limit between the south-westerly monsoon flow and the north-easterly trade winds. In the HL region, radiative cooling (Figure 2(c)) is weak (~ -0.25 K day^{-1}), probably due to the occurrence of mid-level clouds and dust. Above, it is stronger (~ -1 K day^{-1}) and enhances the Hadley-like subsidence.

3.2. *Impact of AEWs on the monsoon state*

As indicated in section 2.2, AEWs are detected according to synoptic dry-to-wet transition events. The reference time t_0 corresponds to the passage of the AEW 600 hPa trough at the

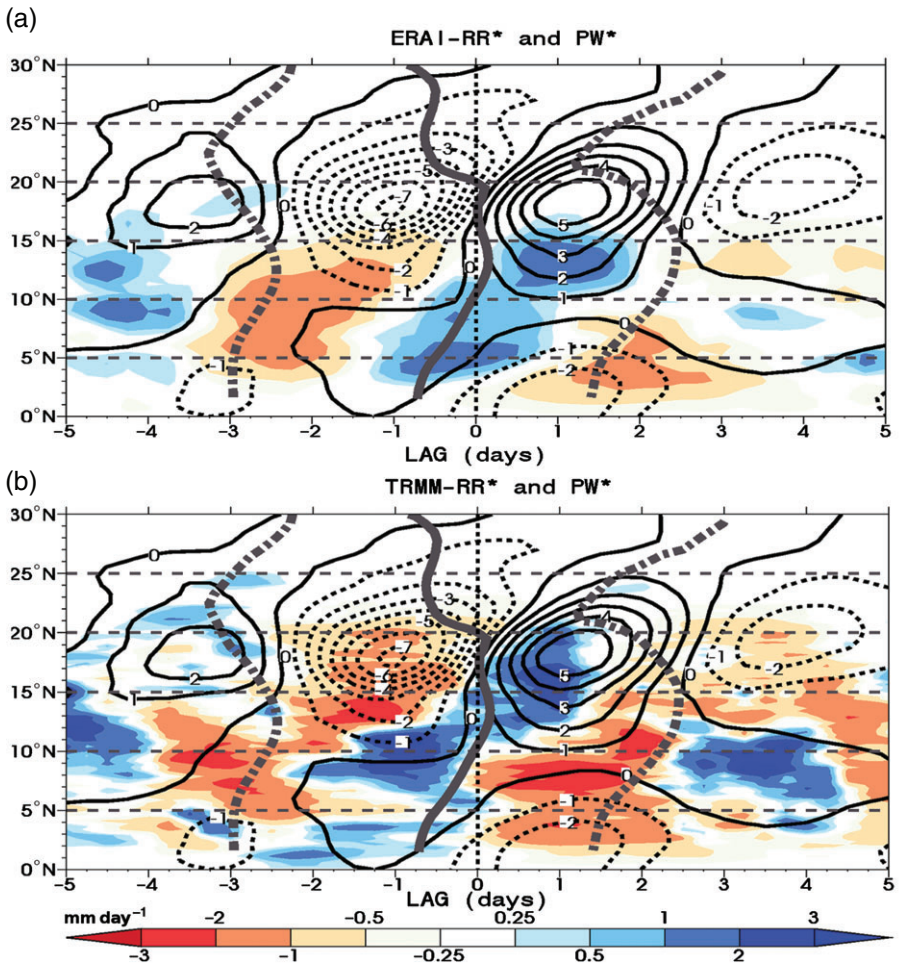

Figure 3. (2°W–2°E) Average latitude–lag evolution of composite rainfall *RR** (mm day^{-1}, colours) and precipitable water *PW** (mm, contours) anomalies. Upper (a) and lower panels (b) are for ERA-I and TRMM *RR** respectively. The bold lines indicate the 600 hPa AEW trough (solid line) and ridge (dashed-dotted line), detected according to the zero contour of 600 hPa meridional wind anomalies.

Greenwich meridian, $t_0 - 1.25$ days corresponds to the dry event and $t_0 + 1.25$ days to the wet event (Figure 3). The occurrence of wet and dry events corresponds to north–south displacement ($\sim \pm 2°$) of the mean monsoon features (Figure 1). Consistent with PRCL13, the maximum PW composite anomalies reach about ±6 mm in the 17–20°N Sahel band, where the mean meridional PW gradient is maximum (Figure 1(b)). During dry events, i.e. ahead of the AEW trough, the HL intensifies and extends further southward (dashed lines, Figure 1(a,c)). The maximum of moist static energy (inferred from the θ_e, Figure 1(d)) retreats southward, consistently with the maximum of precipitation (Figure 1(f)). Opposite patterns occur during wet events, behind (eastward of) the AEW trough. The amplitudes of composite anomalies are mostly symmetric as noted in PRCL13. Although ERA-I rainfall patterns are shifted slightly southward relative to TRMM estimates, rainfall fluctuations during wet and dry events remain consistent between the two datasets (Figure 1(e,f)).

TRMM estimates (Figure 3(b)) indicate a northward propagation of rainfall anomalies from 8 to 20°N at about 7.6 m s^{-1}. The propagation in ERA-I is slower (~5 m s^{-1}), and rainfall anomalies do not extend as far to the north as in TRMM data. South of 12°N, ERA-I rainfall increases in phase with the AEW trough and decreases in phase with the ridge, whereas TRMM estimates anomalies are located rather ahead of the trough and ridge. North of 12°N, TRMM and ERA-I precipitation increases significantly behind the trough, in the southerlies, as shown in earlier studies (Burpee, 1974; Duvel, 1990).

ERA-I thus manages to capture the overall pattern of the coupling between AEWs and convection, but with a few deficiencies as mentioned above. Therefore, some of the following results may depend on the reanalysis used here. Nevertheless, it should be noted that, as discussed in section 2.3, the use of the residual method to estimate apparent sources could reduce errors of the model physics to some extent, as assimilation increments tend to correct them. Also, the use of other reanalyses (or free general circulation models) and other observational datasets in future studies will provide a more in-depth assessment of the robustness of the present results.

3.3. *Modulation of the monsoon circulation and diabatic sources*

Over the Sahel region, the modulations of the WAM features are maximum during the dry and wet phases of AEWs (not shown). The dry phase corresponds to a slight southward retreat of the ITCZ (Figure 4(a)). The subsiding branch of the northern Hadley-like cell intensifies north of 13°N. Underneath this subsiding high layer, the HL ascendant layer also extends southward and reinforces, with intense ascending motions (1.4 cm s^{-1}). The north-easterly trade winds are stronger, whereas the monsoon layer is thinner with a smaller northward extension (ITD at 19°N). The reverse northerly flow above the monsoon flow is also stronger (Figure 4(b)). Conversely, during the AEW wet phase, the ITCZ shifts northward by about 4° and spreads up to 20°N in the upper troposphere as an anvil-like structure (Figure 4(c)). Between 10 and 18°N, subsidence occurs at low level, possibly driven by cooling due to rainfall evaporation. As a result, the heat-low is weakened and pushed northward. The monsoon flow is also deeper and penetrates up to 23°N (ITD), whereas the reverse flow above it almost vanishes (Figure 4(d)). Note that ERA-I radiative heating is not significantly modulated during the life cycle of AEWs.

To further quantify the modulation of diabatic heating and moistening associated with AEWs, Figure 5 depicts vertical

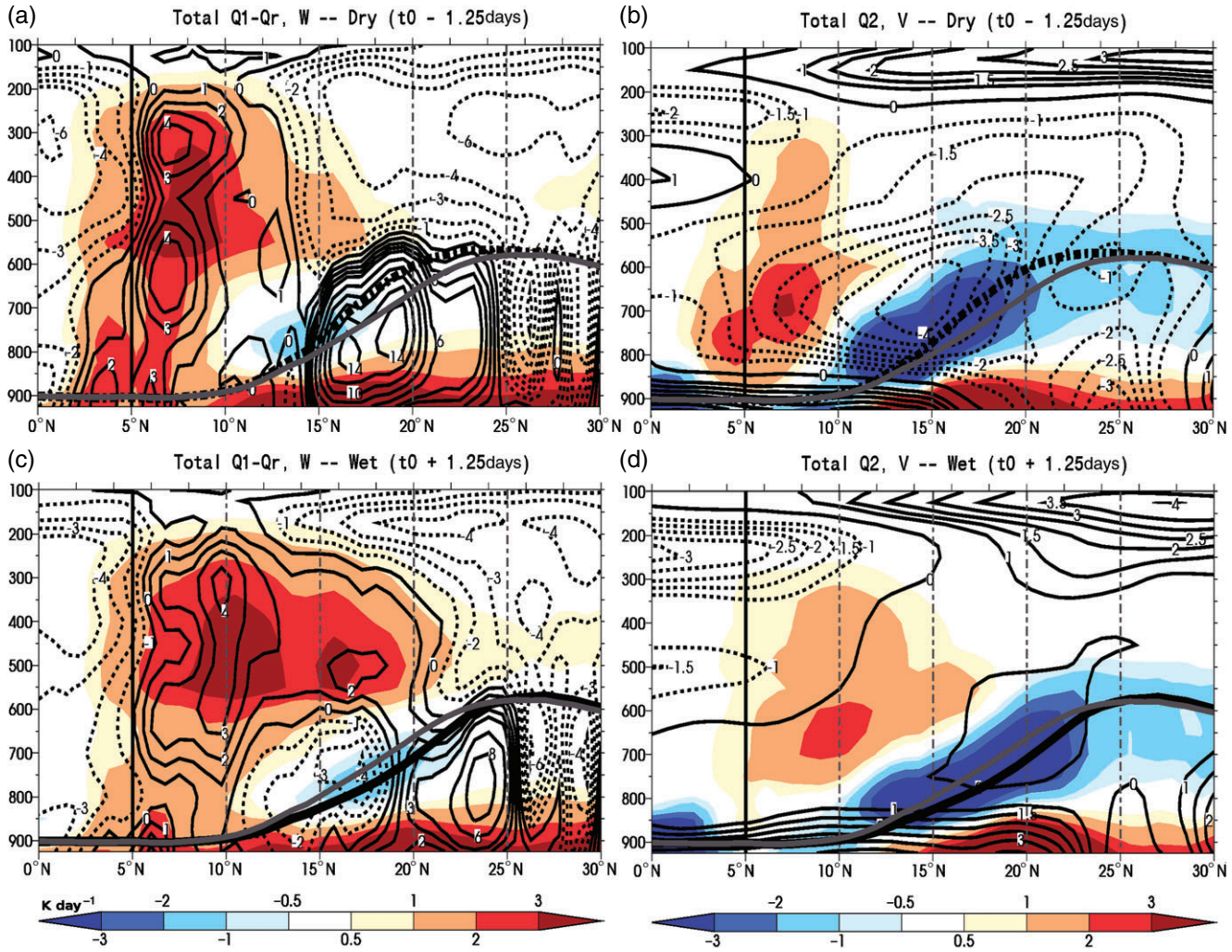

Figure 4. (2°W–2°E) Average meridional vertical cross-section of the AEW composite *dry* (a,b) (t_0- 1.25 days) and *wet* (c,d) (t_0+ 1.25 days) phases. Left column (a,c) is for total $Q_1^{res} - Q_r$ (K day^{-1}, colours) and W(mm s^{-1}, contours). Right column (b,d) is for total Q_2^{res} (K day^{-1}, colours) and V(m s^{-1}, contours). The bold lines indicate the cloud base altitude, for the mean climatology (grey lines) and for the *wet* and *dry* events (solid and dashed-dotted black lines respectively).

profiles of $Q_1^{res} - Q_r$, Q_2^{res} and $Q_1^{res} - Q_r - Q_2^{res}$ at two locations: 7°N (ITCZ) and 17°N (Sahel), for the dry (dashed line) and wet (solid line) phases. At 7°N, diabatic processes heat the whole troposphere (Figure 5(a), thin curves), with a maximum near 550 hPa (∼3 K day^{-1}), consistent with condensation in deep convective clouds. The discontinuity in the 600–550 hPa layer is probably related to melting/freezing processes occurring near the 0 °C layer. During the dry phase, the slight southward retreat of the ITCZ moderately enhances (by 25%) the diabatic heating above 700 hPa. The moisture sink peaks (Figure 5(b)) near 700 hPa. There, the vertical transport by convective and boundary-layer eddies is small ($Q_1^{res} - Q_r - Q_2^{res}$, Figure 5(c)), implying that the drying is the footprint of condensation. At low level, moistening due to boundary-layer transport occurs similarly for both phases, indicating no significant changes in the boundary-layer dynamics in this region.

Over the Sahel at 17°N (Figure 5(a), thick curves), the $Q_1^{res} - Q_r$ profile during the wet phase has a three-layer structure: strong turbulent heating of ∼4 K day^{-1} in the boundary layer, upper-level convective heating above 660 hPa, peaking at ∼3 K day^{-1} at 500 hPa and, between them, cooling reaching −1.5 K day^{-1} at 770 hPa near the cloud base. The latter can be attributed to both rain evaporation and turbulence at the top of and just above the boundary layer. During the dry phase, the more intense heat-low and the increased surface sensible heat flux (not shown) lead to deeper, stronger low-level heating, while the upper-level convective heating is reduced by a factor 3. In between, the cooling layer is also weaker (−50%) and higher, consistently with a higher cloud base (700 hPa). Strong moistening occurs near the cloud base (Figures 4(b,d) and 5(b)) reaching −5 K day^{-1} (∼ +2 g kg^{-1} day^{-1}) during the wet phase, and overhanging strong drying in the lowest layers. During the dry phase, the reinforced heat-low is associated with a deeper boundary layer, moistening a large part of the free troposphere. Conversely, during the wet phase, the boundary layer is shallower and weaker. Above it, convective drying occurs and convection possibly contributes to the moistening of the 850 to 600 hPa layer.

The meridional contrasts in diabatic heating and moistening are remarkable. Meridional heating gradients are thus significantly modulated during the AEW life cycle, which in turn induces changes in the WAM meridional circulation. The impact on the vertical circulation is analysed in the quasi-geostrophic framework in the next subsection.

3.4. *Diabatic heating and vertical circulation within AEWs*

As explained in appendix B, the $\boldsymbol{Q}$ vector can be generalized to account for both adiabatic and diabatic contributions in the omega equation. Divergence of the $\boldsymbol{Q}$ vector indicates subsidence forcing whereas a convergent $\boldsymbol{Q}$ vector indicates ascent forcing. Kiladis *et al.* (2006) found a slight phase lead (one eighth of the AEW period) of convergent $\boldsymbol{Q}$ vectors in the region of vertical velocity maxima, suggesting large-scale dynamical forcing of convection within AEWs. This study also agreed on the inability of the adiabatic vector approach to fully explain the observed vertical motion within AEWs when they occur on the northern side of the AEJ, pointing out the important role of diabatic processes in the AEW energetics. The adiabatic and diabatic contribution to vertical motion in the framework of the $\boldsymbol{Q}$ vector

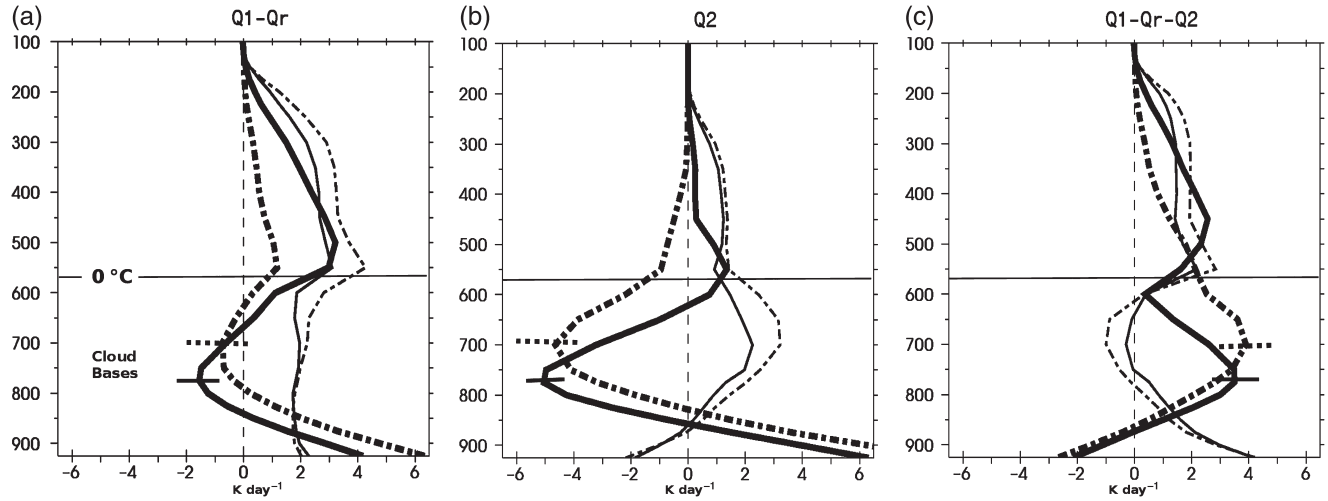

Figure 5. Mean vertical profiles of total (a) $Q_1^{res} - Q_r$, (b) Q_2^{res}, and (c) $Q_1^{res} - Q_2^{res} - Q_r$ for the composite *wet* ($t_0 + 1.25$ days, solid lines) and *dry* ($t_0 - 1.25$ days, dashed-dotted lines) phases, at two locations: for a Sudan point at 7°N (thin lines) and for a Sahel point at 17°N (thick lines), both along the Greenwich meridian. Horizontal bars indicate the cloud base altitudes for the Sahel point.

are shown in Figure 6(a,b) respectively. Note that the shape of the total (adiabatic + diabatic) $\boldsymbol{Q}^*$ vector divergence (not shown) approximates that of vertical velocity anomalies fairly well. The adiabatic contribution is significant only below 700 hPa, where the baroclinicity is large. Consistently with Kiladis *et al.*'s (2006) findings, it shows a slight lead with respect to the vertical velocity anomalies. The diabatic forcing is of similar amplitude and increases more in phase with vertical velocity anomalies. While the adiabatic forcing appears to initiate the vertical circulation of an AEW, the diabatic heating of the boundary-layer processes play a critical role in maintaining it for 1–2 days more.

Above 600 hPa, as horizontal gradients of temperature decrease, the adiabatic forcing vanishes and vertical motion is mostly in equilibrium with the diabatic heating sources. The cooling anomaly during the dry phase induces a large diabatic $\boldsymbol{Q}$ vector divergence and thus a subsidence anomaly. An opposite pattern is observed during the wet phase.

4. Temperature budget over the heat-low southern flank

4.1. *Change of mass and wind fields during AEW passage*

Before the heat budget is analysed, links between mass and wind fields are assessed using latitude–lag composites (Figure 7). The strongest anomalies of mean potential temperature θ^* in the 925 to 600 hPa layer and precipitable water PW^*(Figure 7(a)) are located in the 12–23°N Sahel band, below 600 hPa as shown in PRCL13, where temperature and moisture meridional gradients are maximum. These anomalies are large (±1.5 K, ±6 mm) and anti-correlated, implying that the dry phase of an AEW is also warm and the wet phase is also cool. During the dry phase, the mean-sea-level pressure anomaly is negative and reaches −2 hPa. It is preceded by a strengthening of northerly winds (of −2 m s^{-1}) that push the ITD southward, down to 17°N at t_0− 2.25 days (Figure 7(b)). So, the HL and the associated low-level cyclonic circulation are strongest during the dry phase. After the AEW dry phase (centred on $t_0 - 1.25$ days), southerlies become progressively stronger (more than 3 m s^{-1}), driving a northward penetration of the monsoon flow and the ITD up to 24°N at t_0+ 0.75 days, just before the wet phase (t_0+ 1.25 days). During the wet phase, the HL is weakened (+2 hPa) and an anomalous anticyclonic circulation appears. Following the wet phase, the retreat of the ITD is faster (2 days) consistently with the asymmetry between wet–dry and dry–wet transitions (appendix A).

Above, at the AEJ level (600 hPa), geopotential and circulation anomalies occur with a 1-day lag relative to low-level circulation and pressure anomalies (Figure 7(c)), consistent with the

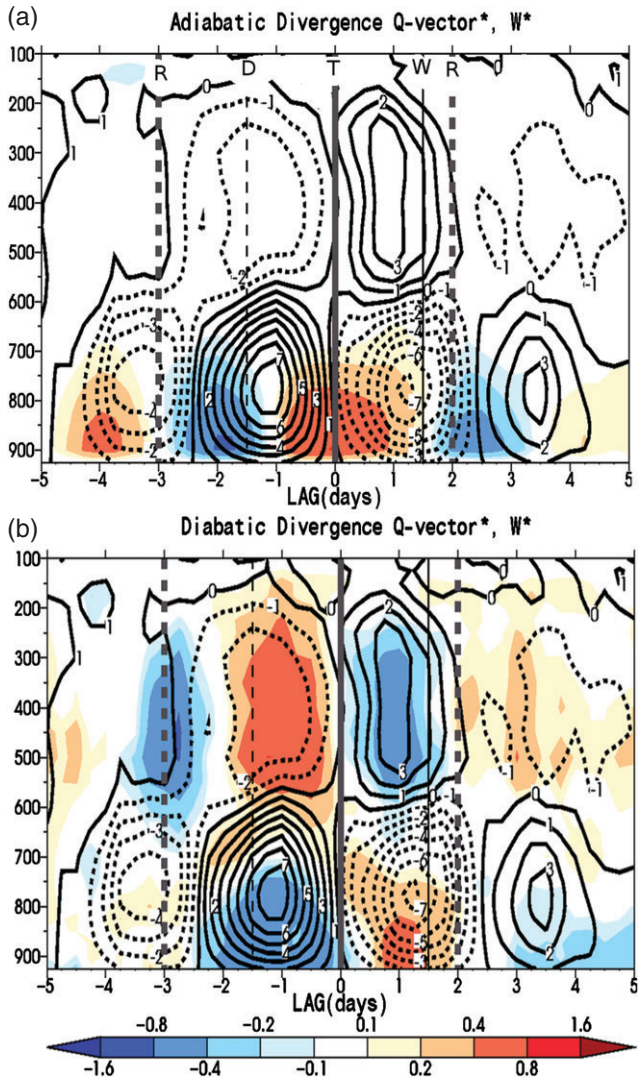

Figure 6. Altitude–lag evolution of $\boldsymbol{Q}^*$ vector divergence ($\times 10^{18}$ Pa^{-1} s^{-3}, colours) and of W^*(mm s^{-1}, contours) average over the Sahel domain (2°W–2°E, 15–20°N) for (a) the adiabatic and (b) the diabatic contributions. Ridge (R), dry (D), trough (T) and wet (W) phases of the composite AEW are indicated with vertical lines.

AEW eastward tilt due to baroclinic conversion. The 600 hPa trough (noted 'T', t_0) corresponds to a geopotential negative anomaly and an anomalous cyclonic circulation. Opposite anomalies occur in the ridge (noted 'R', $t_0 - 3$ or $t_0 + 2$). As at low levels, the T to R transition is faster (2 days)

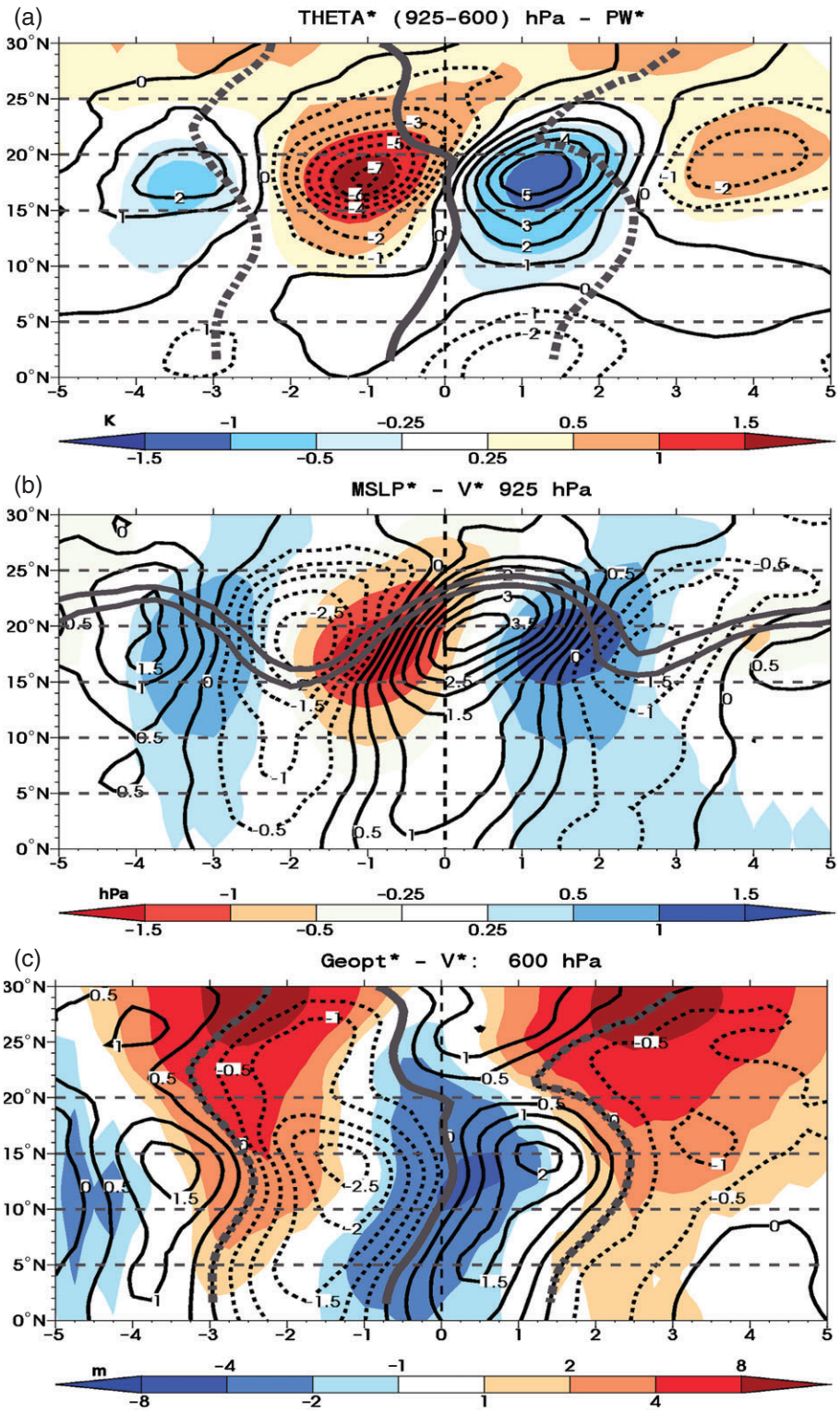

Figure 7. (2°W–2°E) Average latitude–lag composite of (a) mean potential temperature θ^* averaged over the 925 to 600 hPa layer (K, colours) and precipitable water PW^* (mm, contours) anomalies, (b) mean-sea-level pressure MSLP* (hPa, colours) and 925 hPa meridional wind V^*(m s^{-1}, contours) anomalies, and (c) 600 hPa geopotential (m^2 s^{-2}, colours) and 600 hPa meridional wind V^* (m s^{-1}, contours) anomalies. The isocontours of the total meridional wind V at 0 and 1 m s^{-1} superimposed on (b) with bold grey lines indicate the ITD location and its sharpness. The heavy solid and dashed grey lines superimposed on (a) and (c) indicate the AEW trough (T) and ridge (R) at 600 hPa respectively.

than the opposite one (3 days), suggesting that different mechanisms are involved. Consistent with previous studies (Burpee, 1972; Hall *et al.*, 2006; among others), AEW wind anomalies (∼1.5 m s^{-1}) are tilted southwest–northeast to the south of the AEJ axis (∼ 15°N) and in the opposite direction north of the AEJ, in agreement with barotropic energy conversions. The above mass and wind field distributions and their time–space phasing with precipitation over the Sahel are consistent with the results of Taylor *et al.* (2005), although those authors focused their composite study on surface–atmosphere coupling.

Low-level meridional wind anomalies are maximum in the Sahel band but also extend equatorward 1 day earlier, reaching 1 m s^{-1} over the Gulf of Guinea, consistent with the expected pattern of AEW. This is even more evident at 600 hPa, where geopotential and meridional wind anomalies are significant from the Equator to midlatitudes (north of 30°N), suggesting that AEWs presumably interact both with midlatitude and equatorial circulations. This idea is in line with the recent study by Wu *et al.* (2013), which shows possible interactions between the AEJ northern flank, developing AEWs (6–9 day period) and both midlatitude and equatorial weather systems.

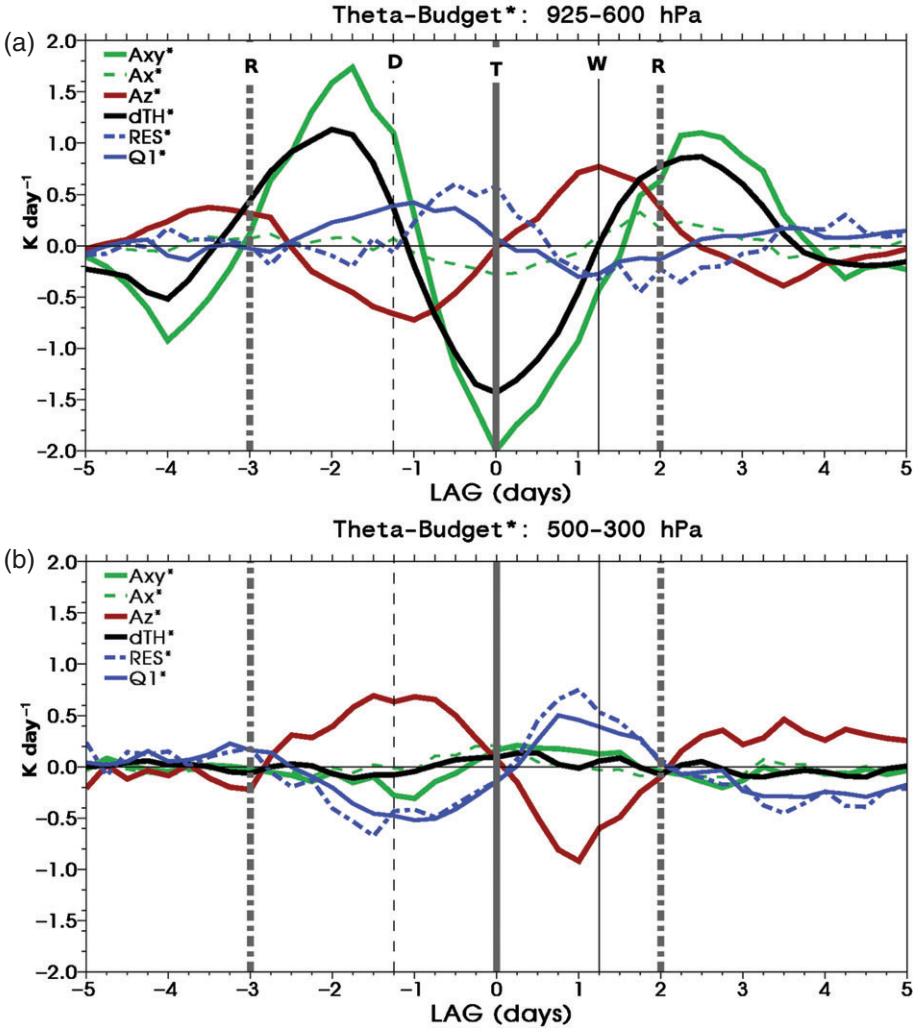

Figure 8. Evolution of the composite budget of the mean potential temperature anomaly (K day^{-1}) in the Sahel box (2°W–2°E, 12–20°N) for (a) the 925–600 hPa layer and (b) the 500–300 hPa layer. Legend shows the contribution of each term of the budget (see text): A_{xy} is the horizontal advection, A_x is the zonal advection, A_z the vertical advection, dTh is the tendency of the potential temperature, RES^* corresponds to Q_1^{res*}, and Q_1^* is the apparent heat source given by ERA-I parametrizations. The vertical lines indicate the AEW 600 hPa trough (T, bold vertical solid line at t_0), ridge (R, dashed-dotted line at t_0- 3 days and t_0+ 2 days), dry phase (D, thin dashed line at t_0- 1.25 days) and wet phase (W, at t_0+ 1.25 days).

4.2. *Temperature budget in the heat-low southern flank*

The present section investigates the AEW heat budget in order to better document the processes at play in the evolution of its thermal structure (Figure 7(a)), especially during the rapid collapse of the HL and its slower recovery. Figure 8 presents the heat budget (various terms of Eq. (1)) for lower and upper levels averaged over (2°W–2°E; 12–20°N), which corresponds to the region of largest temperature anomalies (Figure 7(a)), and the southern part of the HL (Lavaysse *et al.*, 2009) where the composite AEW wave occurs.

Focusing first on the low-level 925 to 600 hPa layer (Figure 8(a)), the collapse of the anomalous HL occurring between the dry and wet phases lasts for 2.25 days. Before and after this collapse, 2.75-day periods are required to recover the anomalous HL. The maximum collapse rate reaches -1.4 K day^{-1} at the trough. Meridional advection of temperature ($A_{xy} - A_x$) is the dominant term of the budget and explains the overall evolution of temperature anomalies, as for the moisture budget (PRCL13). However, the other budget terms are still significant, in particular with regard to their phase shift. Zonal advection (A_x) is weak ($\pm$0.2 K day^{-1}) and slightly precedes meridional advection (see at R). Vertical advection (A_z) is larger ($\pm$0.6 K day^{-1}) and precedes the formation of temperature anomalies. Its magnitude is maximum about 1.5 days before the maximum temperature tendency and is consistent with a large-scale subsidence most intense during the wet phase (cf. Figure 4(c)). Vertical advection thus initiates the HL anomalies and meridional advection then takes over. The HL reaches its maximum intensity during the dry phase. Note that, at that time, vertical advection (large-scale ascendant perturbation) weakens the meridional advection effect. Diabatic heat source anomalies in the HL layer, associated with an increase of the turbulent transport from the boundary layer or/and reduced evaporation of precipitation, partly balance vertical advection, especially during the dry phase. Similar compensation occurs during the wet phase with reduced turbulent mixing and large-scale subsidence. Later, at the trough, the enhanced southerlies result in a strong cooling of the HL that continues up to the wet phase. The estimate of the diabatic heat source depends slightly on the Q_1 retrieval method (section 2.3). Q_1 estimates from ERA-I parametrizations (blue solid line in Figure 8(a)) are in phase with vertical advection and tend to compensate for it, whereas Q_1^{res*} (dotted-dashed blue line in Figure 8(a)) introduces a 0.5-day delay and a greater amplitude.

Above the HL layer, the temperature budget in the 500 to 300 hPa layer mainly corresponds to a balance between vertical advection and diabatic heating (Figure 8(b)): subsiding motion resulting in warming is compensated by a deficit of convective heating during the 3 days around the dry phase and rising motion resulting in cooling is compensated by an excess of convective heating during 2 days around the wet phase. This leads to a weak temperature tendency. Temperature anomalies are small above the AEJ due to the lack of baroclinicity (as shown in PRCL13). The residual method suggests stronger anomalies of the apparent heating source peaking slightly earlier than those derived

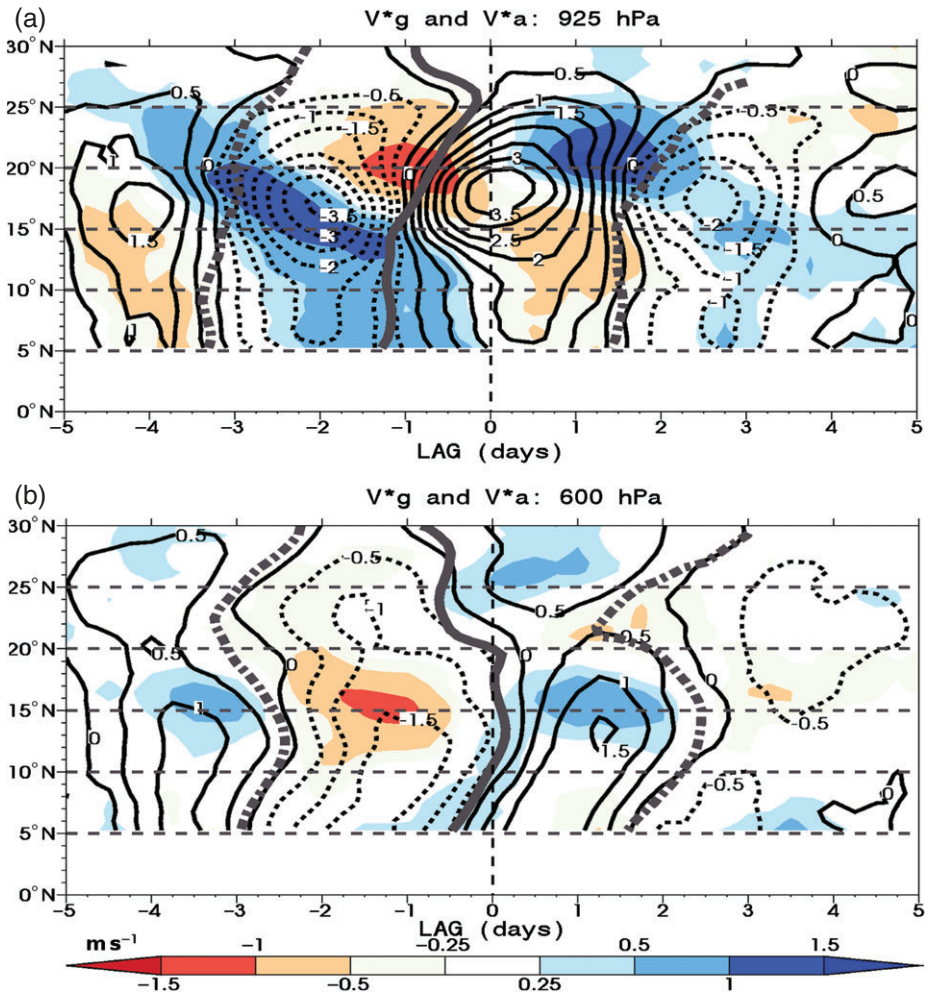

Figure 9. (2°W–2°E) Average latitude–lag composite at (a) 925 hPa and (b) 600 hPa of the geostrophic V_g^* (m s^{-1}, contours) and ageostrophic V_{ag}^* (m s^{-1}, colours) meridional wind anomalies.

from ERA-I physics, consistent with the rainfall composites of Figure (3).

5. Horizontal momentum budget

5.1. *Geostrophic balance*

The preceding analysis indicates that meridional advection of heat and humidity plays a key role (shown in PRCL13) in the AEW life cycle. It also infers strong and complex interactions between large-scale circulation and diabatic processes, with different behaviours below and above the AEJ level. Therefore, there is a need to better document and understand the mechanisms at the origin of wind anomalies, especially for the meridional component. Firstly, it is worthwhile to analyse the degree to which the geostrophic balance can relate wind and mass anomalies, in particular close to the surface (925 hPa, Figure 9(a)) and near the AEJ level (600 hPa, Figure 9(b)).

The geostrophic component of the meridional wind anomalies V_g^* (Figure 9(a,b)) explains the main pattern of the meridional wind anomalies V^* (Figure 7(b,c)). However, the ageostrophic component V_{ag}^* cannot be neglected. At low levels (Figure 9(a)), V_{ag}^* exhibits a complex pattern with opposite effects north and south of 17°N. It is worth noting that these low-level ageostrophic wind convergent/divergent areas are consistent with the adiabatic quasi-geostrophic forcing on the vertical velocity, diagnosed in the previous section 3.4. As suggested by Diaz and Aiyyer (2013a, 2013b), the ageostrophic geopotential fluxes resulting from these strong ageostrophic wind convergent/divergent areas contribute to the local budget of the kinetic energy of the wave and thus to its evolution. Over the northern Sahel, the ageostrophy reinforces the monsoon flow during the wet phase, and thus the northward penetration of the ITD. In the south, V_{ag}^* weakens the monsoon flow. The opposite effect occurs during the dry phase, with an acceleration of northerlies in the north, driving the southward retreat of the ITD and a stronger monsoon flow in the south.

At 600 hPa (Figure 9(b)), the ageostrophic wind anomalies are mainly correlated with their geostrophic counterparts and thus tend to enhance them significantly. In particular, ageostrophy reinforces the 600 hPa cyclonic (anticyclonic) circulation in the AEW trough (ridge).

Few previous studies have discussed the geostrophic imbalance of AEW meridional circulation. Parker (2008) pointed out a meridional surface wind at only 25% of the geostrophic value, whereas our composite shows that it depends on the location, with variation between 50 and 200% of the geostrophic wind. The following section investigates the possible origins of the relatively strong ageostrophic wind. For this purpose, the meridional wind budget is computed and analysed.

5.2. *Meridional momentum budget*

The momentum evolution can be summarized in three terms (Eq. (3)): (i) the total advection A_{xyz}^*, (ii) the sum of the Coriolis and pressure gradient forces, which represents the ageostrophic acceleration *ageo**, and (iii) the apparent source of momentum $Q_{3,y}^{res*}$. These three terms of the meridional momentum budget, together with the meridional wind tendency, are plotted in Figure 10 at 925 and 600 hPa. At both levels, the total advection term plays a minor role, whereas the ageostrophic acceleration and $Q_{3,y}^{res*}$ are dominant terms. The large magnitude of the ageostrophic acceleration confirms the weak geostrophic balance

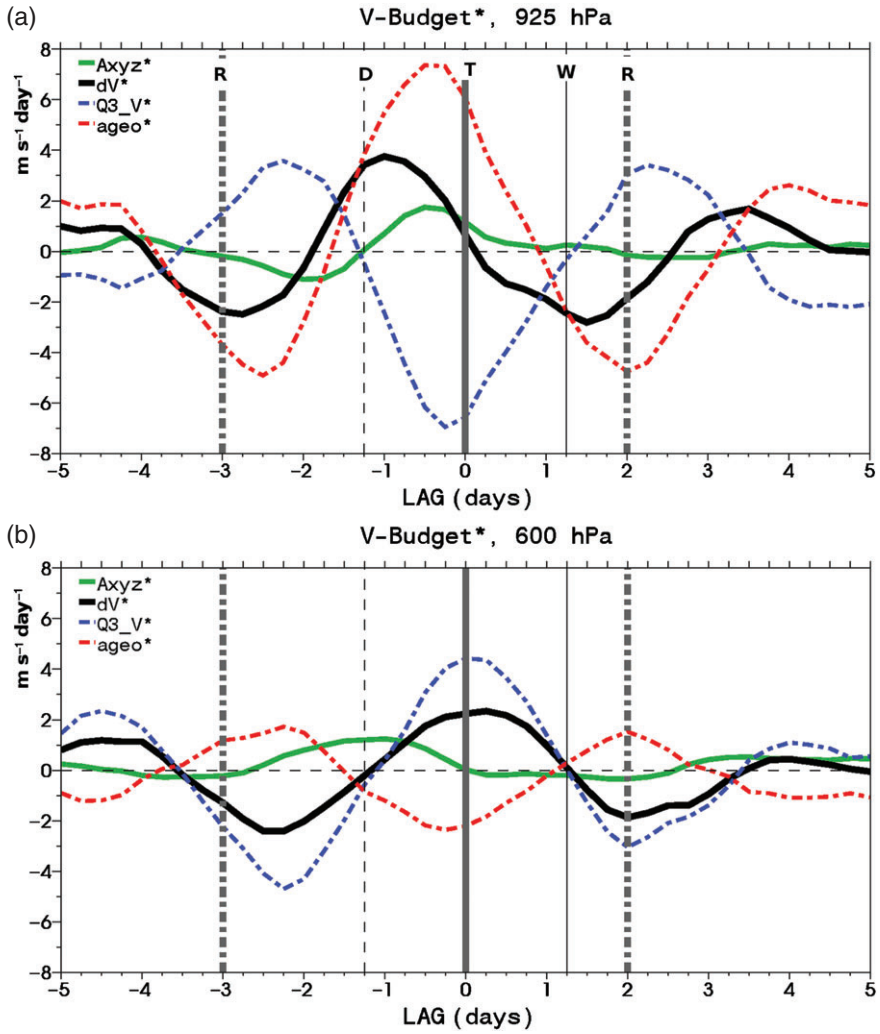

Figure 10. Same as Figure 7 but for the composite budget of the mean meridional momentum anomaly (m s^{-1} day^{-1}) in the Sahel box (2°W–2°E, 12–20°N) at (a) 925 hPa and (b) 600 hPa. $A_{xyz}*$ is the sum of the zonal, meridional and vertical advections, dV^* is the tendency of the meridional wind, *ageo** is the sum of the geopotential term and the Coriolis term. See the text for more details of the different terms.

analysed previously. Near the surface (Figure 10(a)), the monsoon is accelerated northward during the 2 days before the trough T arrives, mainly due to the deepening of the HL (large *ageo** due to the pressure gradient force) as shown by Couvreux *et al.* (2010). The $Q_{3,y}^{res*}$ mostly counterbalances this ageostrophic term with about a 0.5-day lag. As a result, the surface meridional wind acceleration is reduced, and $Q_{3,y}^{res*}$ acts as a strong damping term. The opposite accelerations occur behind the trough.

The amplitude of $Q_{3,y}^{res*}$ is strikingly large, indicating strong vertical transport of wind anomalies by convective and turbulent eddies. It reaches −5 m s^{-1} day^{-1} in the trough at the low level, with the opposite sign at the AEJ level (Figure 10(b)), suggesting large exchanges between these two layers. In short, at 925 hPa, $Q_{3,y}^{res*}$ is intense and acts as a process damping the wind oscillation. Conversely, at 600 hPa (Figure 10(b)), south of 20°N, $Q_{3,y}^{res*}$ is in phase with the meridional wind tendency and thus in quadrature with wind anomalies. It thus enhances the AEW cyclonic circulation and acts as a process that amplifies the wave while the ageostrophic term damps it.

The vertical structures of $Q_{3,y}^{res*}$ and V^* are further documented in Figure 11, at the four phases of AEWs. When the AEW ridge passes over the Greenwich meridian ($t_0 - 3$ days, Figure 11(a)), convection activity is weakened and the monsoon flow is close to its mean state. Nevertheless, $Q_{3,y}^{res*}$ is strong (up to ±3 m s^{-1} day^{-1}) and is characterized by a vertical dipole inducing southward (northward) acceleration above (below) about 850 to 800 hPa. It helps to establish northerlies above 850 hPa and reinforce the HL, which reaches its maximum about 2 days later during the D phase (cf. Figure 7(a)). At this time (Figure 11(b)) northerlies are maximum, the ITD is at 20°N and the monsoon flow is weakest and shallowest. $Q_{3,y}^{res*}$ is now globally positive, with maxima (above 3 m s^{-1} day^{-1}) at mid-levels in the region of reverse wind and north of the ITD at low level. It contributes to the reversal of the northerly anomalies as confirmed about 1 day later at the T passage (Figure 11(c)), since V^* is now positive everywhere up to 600 hPa, resulting in a deeper, stronger monsoon layer reaching 23°N (ITD). Note, however, that the $Q_{3,y}^{res*}$ does not explain the evolution of V^* below 850 hPa, which is mainly explained by the pressure gradient term as shown previously. Also, during the D phase, a deep tower of positive $Q_{3,y}^{res*}$ is noted around 10°N, which may be the trace of the enhanced meridional momentum transport by deep convection at this location. This deep tower reaches 14°N at the T passage, consistent with the northward penetration of the monsoon. At this time, a reverse acceleration develops in the monsoon layer up to 800 hPa, acting as a damping process of the anomalous strong monsoon flux. It is noteworthy that the $Q_{3,y}^{res*}$ field at the passage of T (Figure 11(a)) is almost antisymmetric to one at the passage of R (Figure 11(c)). Another day later, during the W phase (Figure 11(d)), the monsoon starts to retreat and weaken, especially south of 10°N, consistent with the $Q_{3,y}^{res*}$ term. This analysis shows the crucial role of boundary-layer and convective processes in explaining the variations of the meridional wind which, at first order, controls the evolution of PW and heat. Those processes also contribute to the vertically tilted structure of the meridional wind in AEWs. This shows the important coupling between convective processes and AEWs.

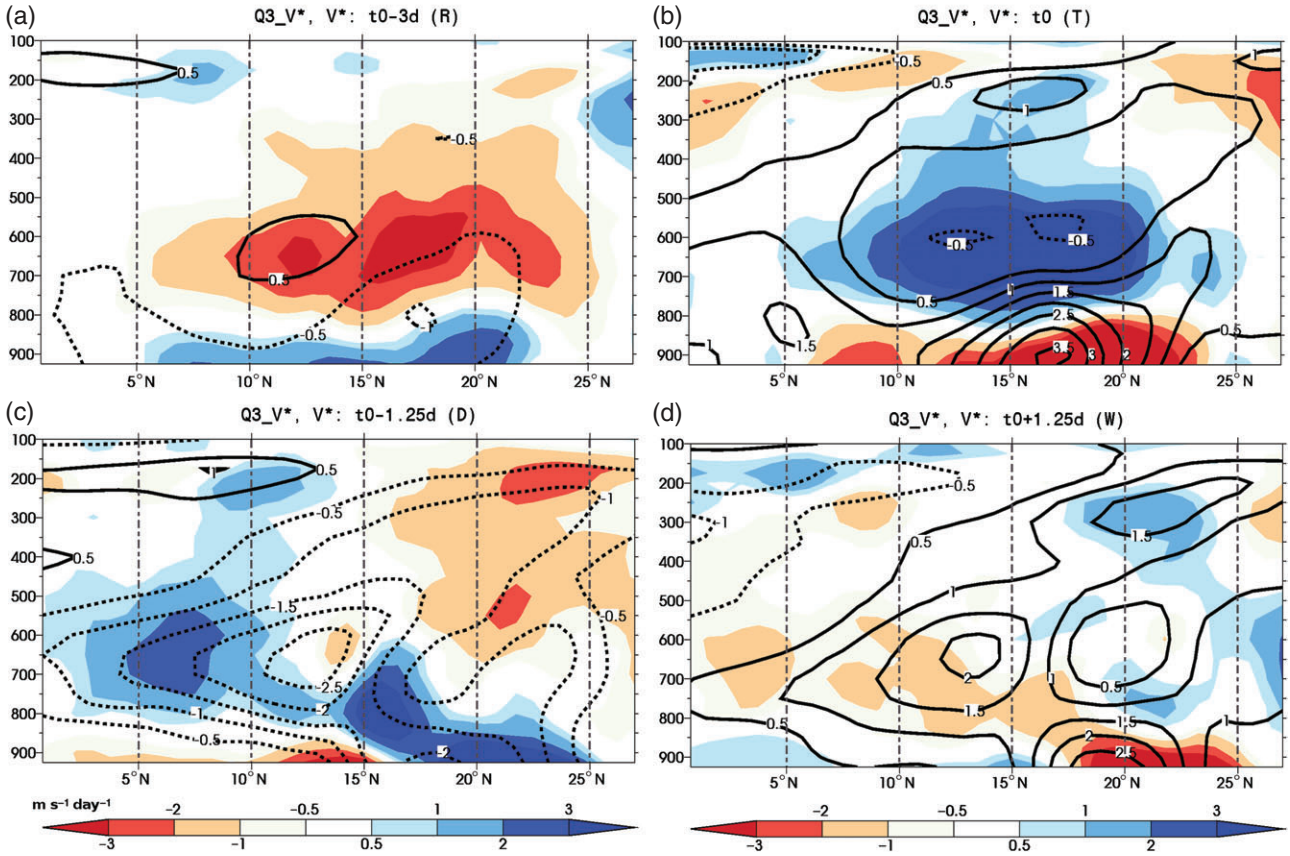

Figure 11. (2°W–2°E) Average meridional vertical cross-section of $Q^*_{3,y}$ (m s^{-1} day^{-1}, colours) and V^* (m s^{-1}, contours) (a) in the ridge (R, t_{0-3} days), (b) during the 'dry' phase (D, t_0 − 1.25 days), (c) in the trough (T, t_0), and (d) during the 'wet' phase (W, t_0 − 1.25 days).

5.3. *Discussion on diabatic momentum transport*

The previous analysis stresses the importance of the apparent source of momentum (meridional component) $Q^{res*}_{3,y}$ in the momentum budget of AEWs, at least in ERA-I reanalysis. However, it is difficult to assess the quality of the present $\mathbf{Q}^{res*}_3$ retrievals with data. Nevertheless, the consistency of the above results and their implications can be discussed in the light of previous studies of momentum transport by convection.

Figure 12 further emphasizes the link between precipitation and the apparent momentum source vector $\mathbf{Q}^{res*}_3$ at 925 and 600 hPa, where it appears to have large amplitudes (cf. Figure 11). Note that the zonal component is now included. The antisymmetric structure of $\mathbf{Q}^{res*}_3$ between the AEW trough and ridge or between the AEW dry and wet phases highlighted in vertical cross-sections (Figure 10) is further confirmed. Figure 12 also highlights concomitance between momentum source and precipitation, especially at 600 hPa (Figure 12(b)), where positive precipitation anomalies correspond to northwestward acceleration by small-scale (subgrid) processes.

Over the Sahel, most of the rainfall is provided by fast-moving squall lines (Mathon *et al.*, 2002b). They are usually oriented north–south, perpendicular to the low-level shear (between surface and 600 hPa). Figure 12(b) thus indicates that the 600 hPa wind is accelerated northward along squall lines, and westward in their normal direction. The westward acceleration is consistent with the up-gradient transport theory of Moncrieff (1992), corresponding to the rear-to-front acceleration generated behind squall lines as derived from observations (Chong *et al.*, 1987; Smull and Houze, 1987) and from high-resolution simulation (Lafore and Moncrieff, 1989; Caniaux *et al.*, 1994b; Diongue *et al.*, 2002). The fact that this rear-to-front acceleration occurs at and below the AEJ level was revealed by vertical cross-sections of $Q^{res*}_{3,x}$ (not shown). It contributes to the acceleration of the AEJ and its shift northward, between the AEW trough and the wet phase. This is consistent with an AEJ core located in the vicinity of the trough, rearward of the enhanced convection areas, as observed by African forecasters. The along-line (north–south) transport has been less studied but seems to simply result from down-gradient transport, as $Q^{res*}_{3,y}$ becomes positive during the dry phase and the trough (Figure 12(b,c)), when precipitation anomalies are positive and vertical shear anomalies negative. The reverse configuration and sources occur during the ridge and wet phase (Figure 12(a,d)). This is in agreement with radar observations and simulations by Barthe *et al.* (2010), who found an apparently along-line source of momentum of ∼1 m s^{-1} h^{-1} comparable with the present values of a few m s^{-1} day^{-1} as convection only lasts a few hours. They also concluded that West African MCSs regionally weaken the low-level monsoon flow and generate southerlies at mid-levels, which enhance the cyclonic circulation within the AEW trough.

At low levels $\mathbf{Q}^{res*}_3$ (Figure 12(a)) is more complex. Its zonal component normal to the squall lines is weak but also westward when precipitation increases. It may be related to cold pools generated through evaporation of convective precipitation, which spread at the surface as density currents. The along-line (meridional) momentum source is opposite to the one at 600 hPa, as shown in Figure 11. It is consistent with suggested down-gradient behaviour, where meridional momentum is transported between low and mid-levels. Nevertheless, at the head of the monsoon flow and north of the ITD, intense $Q^{res*}_{3,y}$ limits the monsoon penetration (retreat) during the wet (dry) phase. This could be related to moist and dry convection, and to small-scale structures in the vicinity of the ITD. Further work is needed both with observations and high-resolution simulations to document the vertical transport of momentum in this region and further confirm its importance in the AEW momentum budget.

6. Conclusion and future work

This study was devoted to the analysis of AEW internal processes involving interactions between convection, mass, dynamics and

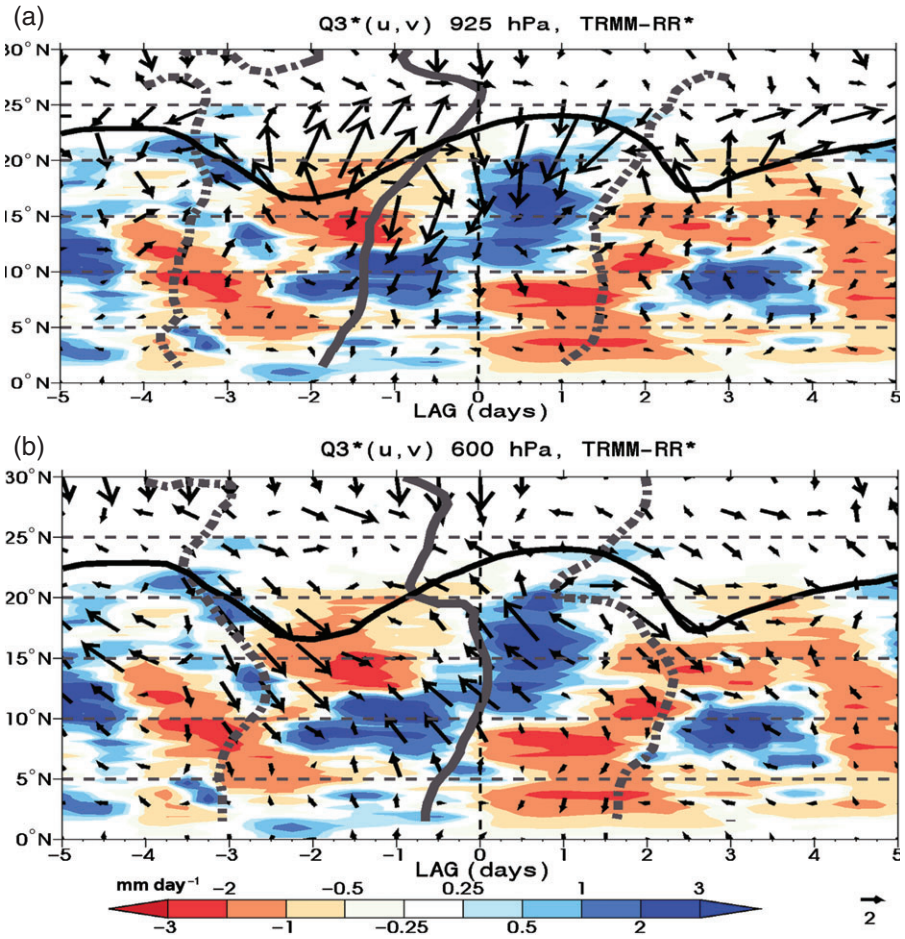

Figure 12. (2°W–2°E) Average latitude–lag evolution of the composite apparent momentum source $\mathbf{Q}_3^{res*}$ vector (m s^{-1} day^{-1}) at (a) 925 hPa and (b) 600 hPa, superimposed on TRMM rainfall composite anomalies (mm day^{-1}, colours).

water vapour fields. The composite analysis was based on synoptic-scale PW anomalies as proposed by PRCL13. However, here, the event selection took the pairs of 'dry' to 'wet' events separated by a time ranging between 1.5 and 3 days into account. This criterion allowed the dispersion in the composite to be reduced by considering events with closer periods. A diagnosis of the impact of convection (dry and moist) within AEWs through the apparent heat and horizontal momentum sources, and humidity sink was addressed using the temperature, momentum and humidity budgets. These were derived from two methods, one using the diagnostic from ERA-I parametrizations and the other employing computation from residuals. Both agree qualitatively but the latter appears to be more consistent in time with the convective activity derived from observations because it takes advantage of the assimilation increment of the reanalysis fields.

For the first time, the interaction between AEW and convective-scale processes has been assessed and analysed throughout the life cycle of the wave. A major result (consistent with Berry and Thorncroft (2012) and Janiga and Thorncroft (2013)) is that barotropic/baroclinic mechanisms alone cannot explain the growth and structure of AEWs. More specifically, this study highlights the crucial role of convective heating in the vertical circulation while adiabatic heat transports generate horizontal circulation by modulating the HL thickness. Convection also appears as a possible mechanism for the vertical wind tilt through its marked subgrid vertical transport of momentum from low levels to mid-levels. It enhances the cyclonic/anticyclonic circulations of the AEW. Figure 13 provides a schematic three-dimensional view of the AEW structure and summarizes the main diabatic processes interacting with the wave that have been highlighted in the present study. First, on the left of Figure 13, the mean meridional vertical cross-section recalls the basic features of the monsoon system averaged over June–September and characterized by: (i) the ITCZ (5–10°N) associated with deep convective heating and mean ascent, (ii) an anvil-type northward extension with heating in the upper levels and cooling underneath, and (iii) north of 15°N, the deep heat-low (HL) with ascent up to ∼600 hPa capped above by the subsiding branch of the northern Hadley cell. The ITD mean position is at ∼20°N in the HL centre. The cloud base rises from 900 to 600 hPa in the Sahel band (∼12–23°N) and marks the strong increase of dryness towards the north. This has a strong impact on Q_1 and Q_2 vertical profiles, favouring cooling and moistening by rain evaporation under convection cells. As the AEW propagates westward while amplifying, at a speed of ∼7–8° day^{-1}, Figure 13 illustrates both its spatial distribution and its temporal evolution during its passage at a given location*. The following scenario is suggested:

- *At the ridge R* (∼20°W, ∼3 days before T passage): the HL starts to intensify due to subsidence (warming) below 600 hPa and the ITD is at its mean position of ∼20°N. Then, meridional advection takes over to strengthen the HL, first by the surface northerlies that become established ahead of the maximum of the HL anomaly (yellow spot) and, a day later, by the reinforcement of northerlies at 600 hPa partly due to the convective eddies. Also, the increase of subsidence above 600 hPa reduces the deep convection, and favours the development of the HL.
- *During the 'dry' stage* (∼1.25 days before T): the HL reaches its maximum at the same time as the northerlies at 600 hPa (large red curved arrow). The planetary boundary layer is deep and very active, and is associated with strong

*We assume a direct transposition here between the temporal evolution studied in this figure and the horizontal distribution.

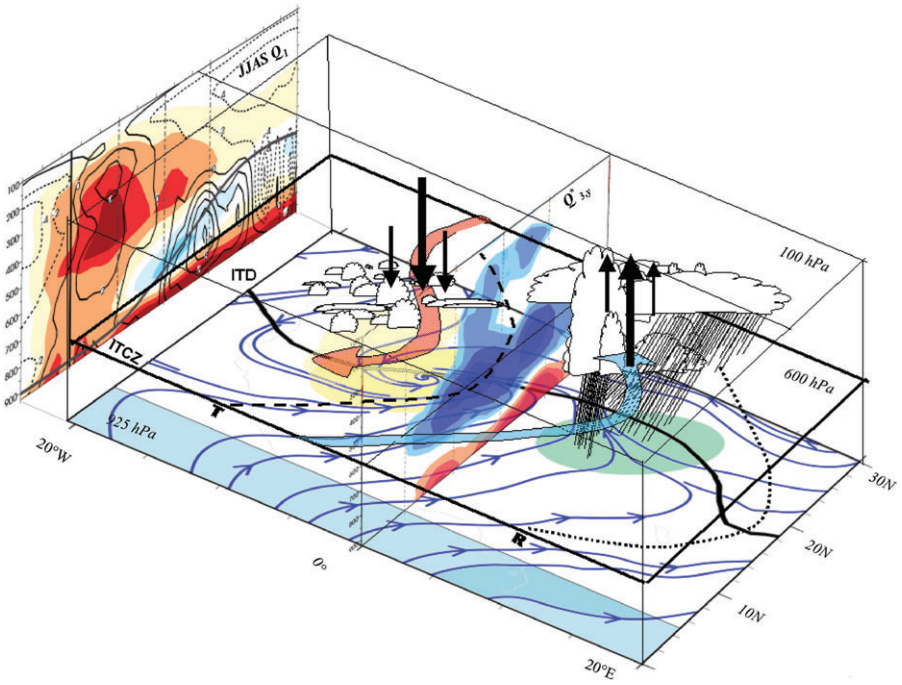

Figure 13. 3D conceptual model of AEW, with the representation of two horizontal cross-sections. The blue streamlines at 925 hPa represent the low-level circulation, with the ITD (bold black line) separating the wet southwest monsoon flow from the warm and dry northerlies. In the Sahel band (12–22°N) the yellow spot represents the dry/warm surface anomalies corresponding to the HL enhancement phase and the green spot represents the wet/cold surface anomalies of the HL weakening. It allows the *dry* (D) and *wet* (W) phases of the AEW to be located. South of 5°N, the blue band represents the ocean in the Gulf of Guinea. The second horizontal plane at the AEJ level (600 hPa) gives the position of the trough (T) just between the dry and wet phases, and the ridge (R). Large red and blue curved arrows represent the northerly and southerly circulation anomalies, respectively, indicating the dynamics of the AEW at 600 hPa. Cloud fields and vertical arrows represent the two opposite regimes of cloud and vertical motion anomalies associated with the dry and wet phases. The latitudinal vertical cross-section at the trough location represents the apparent source of meridional momentum $Q^*_{3,y}$ (i.e. Figure 11(c)). On the western side of the 3D view, the vertical plane represents the mean meridional vertical cross-section in JJAS of $Q_1^{res} - Q_r$ and W (i.e. Figure 1(a)) with the location of the cloud base. This structure propagates westward, while amplifying, at a speed of $\sim 7-8^\circ$ day^{-1}.

subsidence above. In contrast, the ITCZ is reinforced near 10°N (not represented in Figure 13). A low-level cyclonic convergent circulation is generated by the HL, as depicted by the blue streamlines (Figure 13), and results in an acceleration of the monsoon flow in the south-eastern sector of the HL and in a northward progression of the ITD.

- *At the trough T*: northerlies vanish at 600 hPa, while the monsoon flow is maximum due to the surface pressure gradient between the warm and cold anomalies (yellow and green spots respectively). Also the ITCZ progresses northward. The monsoon layer is still thin, so the meridional momentum vertical transport by convection ($Q^{res*}_{3,y}$ vertical slab at T in Figure 13) between the monsoon and the reverse flow above at 600 hPa tends to deepen the monsoon layer by reducing its speed at low level (red area) and accelerating it northward at 600 hPa (blue area).
- *During the 'wet' stage* (∼1.25 day after T): The above conditions are favourable to the generation of a deep, strong monsoon surge resulting in the 'wet' stage. At this time, southerlies at 600 hPa (large blue curved arrow) are maximum over the Sahel. This feeds a deep convection area with strong heating above 600 hPa resulting in a strong ascent anomaly. In contrast, cooling occurs below due to rain evaporation associated with elevated cloud bases (and dry air) and resulting in a subsidence anomaly. In short, the 'wet' stage corresponds to a northward shift of the whole monsoon system (ITCZ, ITD), with a reinforcement of 'anvil' type convection, as highlighted in Figure 5, contributing to the moistening of the northern Sahel.
- *Just after the 'wet' stage*: northerlies are quickly re-established and result in the rapid arrival of a new R only 2 days after the T passage.

In summary, this figure schematically shows the interaction between convection and circulation throughout the AEW life cycle. It should be noted, regarding the 600 hPa geopotential composite (Figure 7(c)), which exhibits large fluctuations up to 30°N, that larger-scale interactions may play an important role in enhancing the northerlies and thus help the AEW organization and growth. This external forcing from midlatitudes has already been suggested (Chauvin *et al.*, 2010; Lavaysse *et al.*, 2010; Wu *et al.*, 2013). Also, in this schematic, the interaction with the surface–atmosphere coupling has not been taken into account, although it should be, as Parker (2008) shows that this is a possible mechanism to explain the westward propagation of AEWs.

ERA-I data allowed us to tackle some aspects of the physics involved in the synoptic variability of the monsoon. However, consistent with previous studies and observations, such physics may depend on the model chosen. Further studies using observations (of radiative and convective heating, surface fluxes and atmosphere thermodynamic profiles), typically from radars and satellites, and also from explicit convective resolved scale models (e.g. CRM) will be useful to validate or improve certain points of our current understanding.

Acknowledgements

The authors are grateful to the anonymous reviewers and the editor for their thoughtful and useful comments on the original manuscript. We also thank Florence Favot for her assistance in computing facilities. Dominique Bouniol has provided some useful comments on the analysis of some results in the light of A-TRAIN satellite observations. ERA-Interim data were provided by the ECMWF. The TRMM 3B42 data were provided by the NASA/Goddard Space Flight Center's Mesoscale Atmospheric Processes Laboratory. The present work was supported by Météo-France, and partly funded by the European Commission's Seventh Framework Programme, under Grant Agreement number 282672, EMBRACE project.

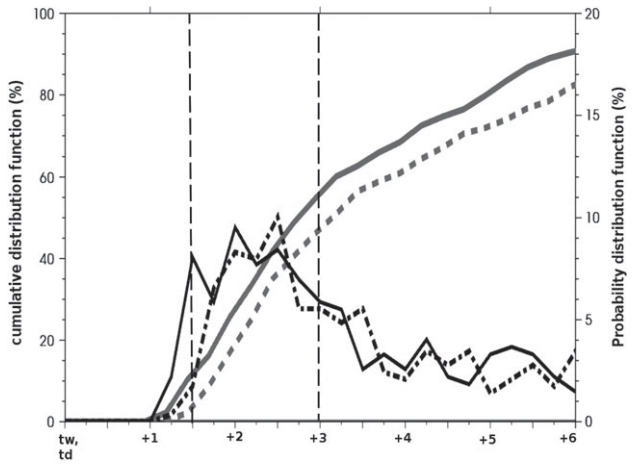

Figure A1. Time–lag probability distribution (in %, scale on the left *y*-axis, black lines) and cumulative distribution function (in %, scale on the right *y*-axis, grey lines) of event occurrence: solid lines are for a dry to wet transition and dashed lines are for the reverse scenario. For a given time reference (t_w or t_d), the lag axis indicates the time it takes to reach the event with the opposite sign. Note that the wet events occurring between 1.5 and 3 days after the dry events (solid lines) will be used for the composites in the present work.

Appendix A

AEWs as transitions between dry and wet synoptic events

Among the wet and dry events detected and analysed in PRCL13, some can be considered as isolated, meaning that they are not preceded or followed by a strong anomaly of precipitable water within a time window of a few days. These events contribute to the spread in the composite analysis while, in an idealized or canonical AEW, the trough is expected to be surrounded by a dry event and a wet event. Figure A1 quantifies the frequency of occurrence of transitions between wet and dry events, as seen by the probability and cumulative distribution functions (PDF and CDF) of the time separation between consecutive wet and dry events. When such a transition occurs, it corresponds to a strong AEW, at least in terms of its moisture footprint. There is a high probability of a dry event being followed by a wet event within 3 days (55% as seen on the cumulative distribution function). The same is true for the occurrence of a wet-to-dry transition event within 3 days (∼50%). The maximum of the PDF is slightly delayed in the case of dry-to-wet transitions (2.5 days, dashed curve) compared to that of wet to dry sequences (2 days, solid curve), implying possible differences in their physics.

To maximize the signal-to-noise ratio in the composite analysis, especially in the perspective of analysing diabatic processes but also to change from a perspective of synoptic dry and wet events to the AEW perspective, only the most probable transition events are considered in the present study. Dry-to-wet transition events are defined as a sequence of a dry event followed by a wet event within 1.5–3 days[†]. This transition event is detected by the date just between the dry and wet event and corresponds to the mid-level trough of the associated AEW. The CDF (Figure A1) indicates that about 40% of all dry events are kept for the composite analysis and that about one dry-to-wet transition event is detected per month. Note that wet-to-dry transition events are defined in the same manner and correspond to the mid-level ridge of the associated AEW. They lead to mostly symmetrical results.

Appendix B

Diabatic heat source and quasi-geostrophic *Q* vector formulation

In the quasi-geostrophic approximation, the divergence of the classic $\mathbf{Q}$ vector is one of the source terms in the omega equation (Holton, 2004) and can be seen as an adiabatic contribution to the vertical motions. Computing this source term of vertical velocity, Kiladis *et al.* (2006) showed that it accounts for part of the forcing. Here, we propose to use a generalized version of this $\mathbf{Q}$ vector in which the diabatic heating source of vertical velocity can be added. Following the approximations of Kiladis *et al.* (2006), and in the context of the composite approach, the divergence of the $\mathbf{Q}$ vector reads:

$$\nabla\cdot\mathbf{Q}^* = \nabla\cdot\mathbf{Q}_a^* + \nabla\cdot\mathbf{Q}_d^* \approx -\frac{R}{p}\pi\frac{\partial\bar{\theta}}{\partial y}\frac{\partial\zeta^*}{\partial x} - \frac{R}{p}\left\{\frac{\partial}{\partial x}\left(\frac{\partial(Q_1^{res})^*}{\partial x}\right)+\frac{\partial}{\partial y}\left(\frac{\partial(Q_1^{res})^*}{\partial y}\right)\right\}$$

where R is the gas constant for dry air, θ and ζ^* are respectively the mean potential temperature and the composite vorticity anomaly at a given level p, and Q_1^{res*} is the apparent heat source derived in section 3.

References

Barthe C, Asencio N, Lafore J-P, Chong M, Campistron B, Cazenave F. 2010. Multi-scale analysis of the 25–27 July 2006 convective period over Niamey: Comparison between Doppler radar observations and simulations. *Q. J. R. Meteorol. Soc.* **136**: 190–208.

Berry GJ, Thorncroft CD. 2005. Case study of an intense African easterly wave. *Mon. Weather Rev.* **133**: 752–766.

Berry GJ, Thorncroft CD. 2012. African easterly wave dynamics in a mesoscale numerical model: The upscale role of convection. *J. Atmos. Sci.* **69**: 1267–1283.

Burpee RW. 1972. The origin and structure of easterly waves in the lower troposphere of North Africa. *J. Atmos. Sci.* **29**: 77–90.

Burpee RW. 1974. Characteristics of North African easterly waves during the summers of 1968 and 1969. *J. Atmos. Sci.* **31**: 1556–1570.

Caniaux G, Redelsperger J-L, Lafore J-P. 1994a. A numerical study of the stratiform region of a fast-moving squall line. Part I: General description and water and heat budgets. *J. Atmos. Sci.* **51**: 2046–2074.

Caniaux G, Lafore J-P, Redelsperger J-L. 1994b. A numerical study of the stratiform region of a fast-moving squall line. Part II: Relationship between mass, pressure and momentum fields. *J. Atmos. Sci.* **52**: 331–352.

Chauvin F, Roehrig R, Lafore J-P. 2010. Intraseasonal variability of the Saharan Heat Low and its link with mid-latitudes. *J. Clim.* **23**: 2544–2561.

Chong M, Amayenc P, Scialom G, Testud J. 1987. A tropical squall line observed during the COPT81 experiment in West Africa. Part I: Kinematic structure inferred from dual-Doppler radar data. *Mon. Weather Rev.* **115**: 670–694.

Cornforth R, Thorncroft CD, Hoskins BJ. 2009. The impact of moist processes on the African easterly jet–African easterly wave system. *Q. J. R. Meteorol. Soc.* **135**: 894–913.

Couvreux F, Guichard F, Bock O, Campistron B, Lafore J-P, Redelsperger J-L. 2010. Synoptic variability of the monsoon flux over West Africa prior to the onset. *Q. J. R. Meteorol. Soc.* **136**: 160–174.

Cuesta J, Lavaysse C, Flamant C, Mimouni M, Knippetz P. 2010. Northward bursts of the West African monsoon leading to rainfall over the Hoggar massif, Algeria. *Q. J. R. Meteorol. Soc.* **136**: 174–189, doi: 10.1002/qj.439.

Dee DP, Uppala SM, Simmons AJ, Berrisford P, Poli P, Kobayashi S, Andrae U, Balmaseda MA, Balsamo G, Bauer P, Bechtold P, Beljaars ACM, van de Berg L, Bidlot J, Bormann N, Delsol C, Dragani R, Fuentes M, Geer AJ, Haimberger L, Healy SB, Hersbach H, Hólm EV, Isaksen L, Kållberg P, Köhler M, Matricardi M, McNally AP, Monge-Sanz BM, Morcrette J-J, Park B-K, Peubey C, de Rosnay P, Tavolato C, Thépaut J-N, Vitart F. 2011. The ERA-Interim reanalysis: Configuration and performance of the data assimilation system. *Q. J. R. Meteorol. Soc.* **125**: 553–597, doi: 10.1002/qj.828.

Diaz ML, Aiyyer A. 2013a. Energy dispersion in African easterly waves. *J. Atmos. Sci.* **70**: 130–145, doi: 10.1175/JAS-D-12-019.1.

Diaz M, Aiyyer A. 2013b. The genesis of African easterly waves by upstream development. *J. Atmos. Sci.* **70**: 3492–3512, doi: 10.1175/JAS-D-12-0342.1.

Di Giuseppe F, Molteni F, Dutra E. 2013. Real-time correction of ERA-I monthly rainfall. *Geophys. Res. Lett.* **40**: 1–6, doi: 10.1002/grl.50670.

Diongue A, Lafore JP, Redelsperger JL, Roca R. 2002. Numerical study of a Sahelian synoptic weather system: Initiation and mature stages of convection and its interactions with the large-scale dynamics. *Q. J. R. Meteorol. Soc.* **128**: 1899–1927.

Duvel JP. 1990. Convection over tropical Africa and the Atlantic Ocean during northern summer. Part II: Modulation by easterly waves. *Mon. Weather Rev.* **118**: 1855–1868.

Fink AH. 2012. 'To the 75th anniversary of the discovery of African Easterly Waves'. In *30th Conference on Hurricanes and Tropical Meteorology*. Ponte Vedra Beach, FL, S3.1. Extended Abstract: http://ams.confex.com/ams/30Hurricane/webprogram/Manuscript/Paper206073/extended_

[†]The sensitivity of the composite analysis to the exact range of delays between wet and dry events remains weak.

abstrext_30stamshurr_2012_fink_AEWhistory.pdf (accessed 15 March 2012).

Fink AH, Reiner A. 2003. Spatio-temporal variability of the relation between African easterly waves and West African squall lines in 1998 and 1999. *J. Geophys. Res.* **108**: 4332, doi: 10.1029/2002JD002816.

Hall NMJ, Kiladis GN, Thorncroft CD. 2006. Three-dimensional structure and dynamics of African easterly waves. Part II: Dynamical modes. *J. Atmos. Sci.* **63**: 2231–2245.

Holton JR. 2004. *An Introduction to Dynamic Meteorology* (4th edn). Elsevier Academic Press: Amsterdam.

Hubert H. 1939. Origine africaine d'un cyclone tropical atlantique. *Ann. Phys. France d'Outre-Mer* **6**: 97–115.

Huffman GJ, Adler RF, Boldin DT, Gu G, Nelkin EJ, Bowman KP, Hong Y, Stocker EF, Wolff DB. 2007. The TRMM multi-satellite precipitation analysis: Quasi-global, multi-year, combined-sensor precipitation estimates at fine scale. *J. Hydrometeorol.* **8**: 38–55.

Janiga MA, Thorncroft CD. 2013. Regional differences in the kinematic and thermodynamic structure of African easterly waves. *Q. J. R. Meteorol. Soc.* **139**: 1598–1614.

Kiladis GN, Thorncroft CD, Hall NMJ. 2006. Three-dimensional structure and dynamics of African easterly waves. Part I: Observations. *J. Atmos. Sci.* **63**: 2212–2230.

Lafore J-P, Moncrieff MW. 1989. A numerical investigation of the organization and interaction of the convective and stratiform regions of tropical squall lines. *J. Atmos. Sci.* **46**: 521–544.

Lafore J-P, Flamant C, Giraud V, Guichard F, Knippertz P, Mahfouf J-F, Mascart P, Williams ER. 2010. Introduction to the AMMA special issue on 'Advances in understanding atmospheric processes over West Africa through the AMMA field campaign'. *Q. J. R. Meteorol. Soc.* **136**: 2–7, doi: 10.1002/qj.583.

Lavaysse C, Flamant C, Janicot S, Parker DJ, Lafore J-P, Sultan B, Pelon J. 2009. Seasonal evolution of the West African heat low: A climatological perspective. *Clim. Dyn.* **33**: 313–330, doi: 10.1007/s00382-009-0553-4.

Lavaysse C, Flamant C, Janicot S, Knippertz P. 2010. Links between African easterly waves, midlatitude circulation and intraseasonal pulsations of the West African heat low. *Q. J. R. Meteorol. Soc.* **136**: 141–158.

Leroux S, Hall NMJ. 2009. On the relationship between African easterly waves and the African Easterly Jet. *J. Atmos. Sci.* **66**: 2303–2316.

Mathon V, Diedhiou A, Laurent H. 2002a. Relationship between easterly waves and mesoscale convective systems over the Sahel. *Geophys. Res. Lett.* **29**: 571–574, doi: 10.1029/2001GL014371.

Mathon V, Laurent H, Lebel T. 2002b. Mesoscale convective system rainfall in the Sahel. *J. Appl. Meteorol.* **41**: 1081–1092.

Mekonnen A, Thorncroft CD, Aiyyer A. 2006. Analysis of convection and its association with African easterly waves. *J. Clim.* **19**: 5405–5421.

Moncrieff MW. 1992. Organized convective systems: Archetypal dynamical models, mass and momentum flux theory, and parametrization. *Q. J. R. Meteorol. Soc.* **118**: 819–850.

Paradis D, Lafore JP, Redelsperger JL, Balaji V. 1995. African easterly waves and convection. Part I: Linear simulations. *J. Atmos. Sci.* **52**: 1657–1679.

Parker DJ. 2008. A simple model of coupled synoptic waves in the land surface and atmosphere of the northern Sahel. *Q. J. R. Meteorol. Soc.* **134**: 2173–2184.

Piersig W. 1936. Schwankungen von Luftdruck und Luftbewegung sowie ein Beitrag zum Wettergeschehen im Passatgebiet desöstlichen Nordatlantischen Ozeans (in German). *Arch. Deut. Seewarte* **54**: Nr. 6.

Poan DE, Roehrig R, Couvreux F, Lafore J-P. 2013. West African monsoon intraseasonal variability: A precipitable water perspective. *J. Atmos. Sci.* **70**: 1035–1052, doi: 10.1175/JAS-D-12-087.1.

Pytharoulis I, Thorncroft C. 1999. The low-level structure of African easterly waves in 1995. *Mon. Weather Rev.* **127**: 2266–2280.

Redelsperger JL, Lafore J-P. 1994. Non-hydrostatic simulations of a cold front observed during the FRONTS-87 experiment. *Q. J. R. Meteorol. Soc.* **120**: 519–555.

Reed RJ, Norquist DC, Recker EE. 1977. The structure and properties of African wave disturbances as observed during phase III of GATE. *Mon. Weather Rev.* **105**: 317–333.

Regula H. 1936. Druckschwankungen und Tornados an der Westküste von Afrika. *Ann. Hydrogr. Maritimen Meteorol.* **64**: 107–111.

Riehl H. 1954. Waves in the easterlies. In *Tropical Meteorology*, Chapter 9, Riehl H. (ed.): 210–234. McGraw-Hill: New York, NY.

Roca R, Chambon P, Jobard I, Kirstetter P-E, Gosset M, Bergés J-C. 2010. Comparing Satellite and Surface Rainfall Products over West Africa at Meteorologically Relevant Scales during the AMMA Campaign Using Error Estimates. *J. Appl. Meteor. Climatol.* **49**: 715–731, doi: http://dx.doi.org/10.1175/2009JAMC2318.1.

Smull BF, Houze RA Jr. 1987. Rear inflow in squall lines with trailing stratiform precipitation. *Mon. Weather Rev.* **115**: 2869–2889.

Taylor CM, Parker DJ, Lloyd CR, Thorncroft CD. 2005. Observations of synoptic-scale land surface variability and its coupling with the atmosphere. *Q. J. R. Meteorol. Soc.* **131**: 913–938.

Thorncroft CD, Blackburn M. 1999. Maintenance of the African Easterly Jet. *Q. J. R. Meteorol. Soc.* **125**: 763–786.

Thorncroft CD, Hoskins BJ. 1994a. An idealized study of African easterly waves. I: A linear view. *Q. J. R. Meteorol. Soc.* **120**: 953–982.

Thorncroft CD, Hoskins BJ. 1994b. An idealised study of African easterly waves. II: A nonlinear view. *Q. J. R. Meteorol. Soc.* **120**: 983–1015.

Thorncroft CD, Parker DJ, Burton RR, Diop M, Ayers JH, Barjat H, Devereau S, Diongue A, Dumelow R, Kindred DR, Price NM, Saloum M, Taylor CM, Tompkins AM. 2003. The JET2000 project: Aircraft observations of the African easterly jet and African easterly waves. *Bull. Am. Meteorol. Soc.* **84**: 337–351.

Wu M-LC, Reale O, Schubert SD. 2013. A characterization of African easterly waves on 2.5–6-day and 6–9-day time scales. *J. Clim.* **26**: 6750–6774, doi: 10.1175/JCLI-D-12-00336.1.

Yanai M, Esbensen S, Chu JH. 1973. Determination of bulk properties of tropical cloud clusters from large-scale heat and moisture budgets. *J. Atmos. Sci.* **30**: 611–627.

